

**NUCLEAR REACTOR PROGRAM  
NC STATE UNIVERSITY**

**USER GUIDE**

**CONTACT INFORMATION:**

**Ayman Hawari, Director**

email: [Ayman.Hawari@ncsu.edu](mailto:Ayman.Hawari@ncsu.edu)

Ph: (919)515-4598

**Scott Lassell, Nuclear Services Manager**

email: [salassel@ncsu.edu](mailto:salassel@ncsu.edu)

Ph: (919)515-3347

**NRP Website:** <http://www.ne.ncsu.edu/nrp/index.html>

**Facility Address:**

2500 Stinson Drive, Rm.#2117 Burlington Lab, Raleigh, NC 27695-7909

**Table of Contents**

	<u>Page</u>
<b>1. Nuclear Reactor Program .....</b>	<b>2</b>
<b>2. PULSTAR Reactor .....</b>	<b>3</b>
<b>2.1</b> Reactor Description .....	<b>3</b>
<b>2.2</b> Reactor Power Uprate Project .....	<b>5</b>
<b>2.3</b> PULSTAR Facility Capabilities .....	<b>8</b>
<b>3. User Facility Descriptions</b>	
<b>3.1</b> Neutron Powder Diffraction Facility and Microstructure Analysis Laboratory..	<b>10</b>
<b>3.2</b> Neutron Imaging Facility .....	<b>17</b>
<b>3.3</b> Positron Intense Beam Facility and Defect Analysis Laboratory .....	<b>23</b>
<b>3.4</b> Ultra Cold Neutron Source .....	<b>30</b>
<b>3.5</b> Internet Reactor Laboratory .....	<b>33</b>
<b>3.6</b> Neutron Activation Analysis .....	<b>36</b>
<b>3.7</b> Reactor Irradiations and Isotope Production .....	<b>39</b>
 <b>Appendices:</b>	
<b>A.</b> Analysis of Nuclear Graphite using the Neutron Powder Diffraction Facility and Microstructure Analysis Laboratory .....	<b>42</b>
<b>B.</b> Characterization of Defects in Nuclear Graphite Using the Positron Intense Beam Facility and Defect Analysis Laboratory .....	<b>52</b>

## 1. Nuclear Reactor Program

The Nuclear Reactor Program (NRP) is a University Center that operates within the Department of Nuclear Engineering at North Carolina State University. The NRP administers the PULSTAR Reactor Laboratory with the mission of enhancing, promoting and utilizing the reactor and associated facilities for the purposes of education, scientific discovery, and outreach. The PULSTAR is the latest of four research reactors built at NC State by the nation's first academic nuclear engineering program established in 1950. The 1 MW PULSTAR (see Figure 1.1), which went critical in 1972, is the largest of the reactors built to date, and has a suite of state-of-the-art research and testing capabilities.

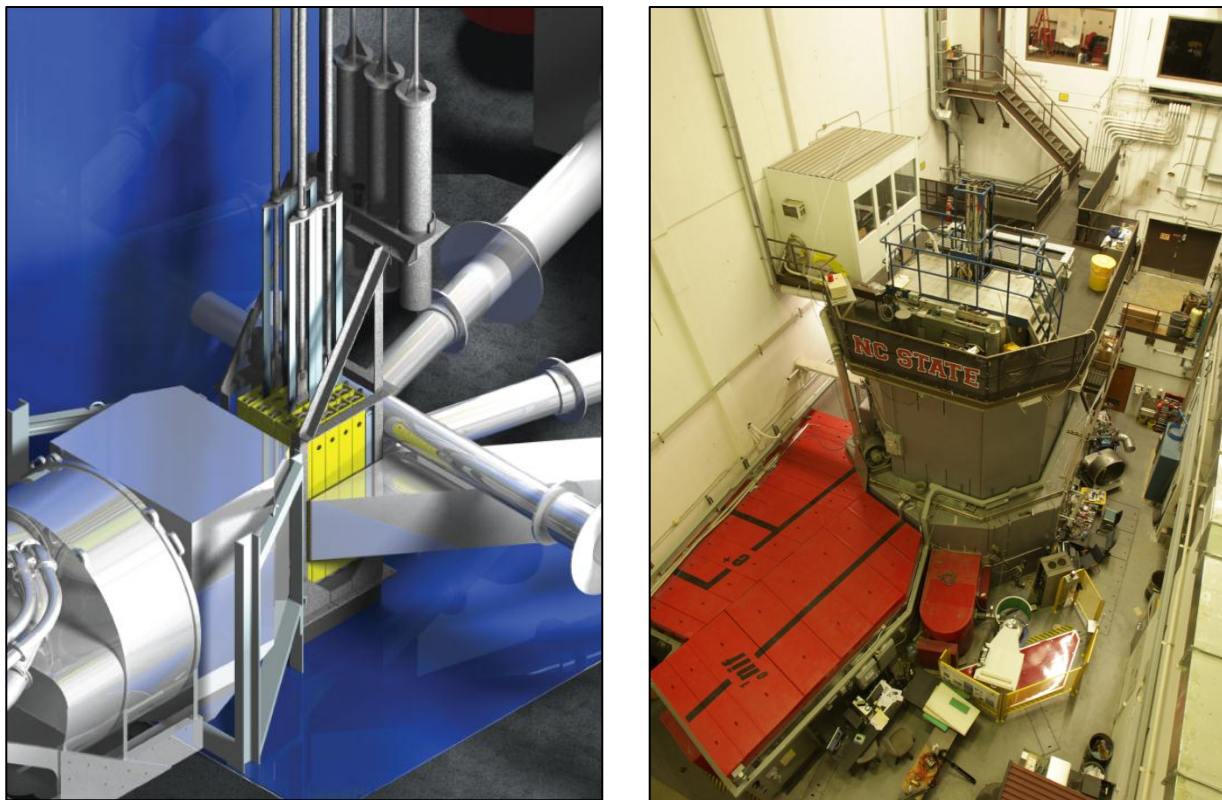


**Fig. 1.1 – PULSTAR Reactor Core schematic (left) and reactor bay and experiment floor (right).**

The reactor and experimental facilities are available for use by domestic and international academic, corporate, and government users. The NRP Nuclear Services Center facilitates all utilization of the reactor by external parties and serves as the primary point of contact for users.

## 2. PULSTAR Reactor

### 2.1 Reactor Description

The PULSTAR represents an open pool and light water moderated and cooled reactor that is fueled with uranium dioxide ( $UO_2$ ) enriched to 4% in U-235. The fuel is configured into assemblies that contain 25 fuel pins each and are arranged in a square  $5 \times 5$  array. The fuel pins are clad with Zircaloy 2 cladding. The core contains 25 assemblies that are arranged in a  $5 \times 5$  square array. In addition, four Ag-In-Cd control rod blades are utilized in the core. Figure 2.1 shows a schematic of the PULSTAR core and a cutaway of a typical fuel assembly.

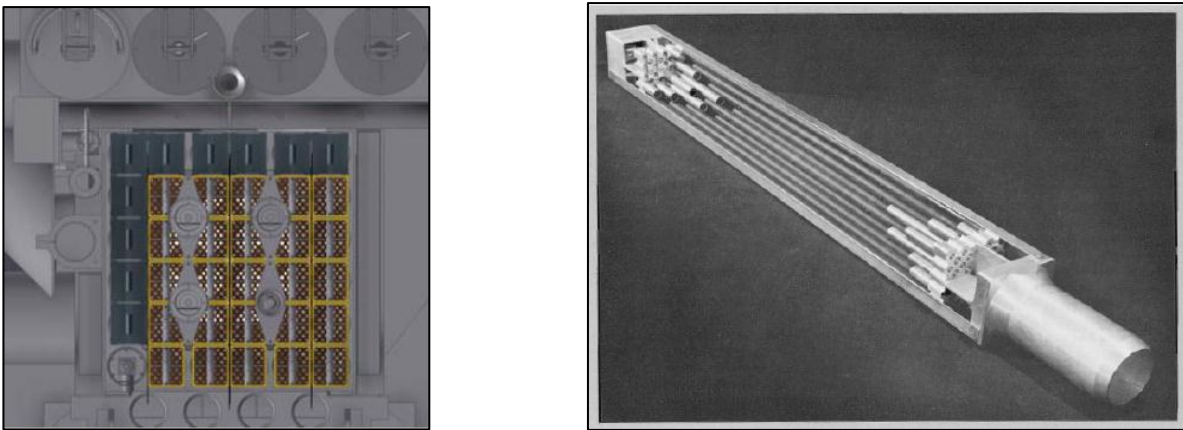


**Fig. 2.1 - A top view of the current PULSTAR core (left) and a cutaway of a typical fuel assembly (right).**

To enhance the core's neutron economy and to extend its lifetime, beryllium reflectors are used on two sides of the core. For utilization purposes, vertical irradiation access tubes are placed at the core periphery and are routinely used in materials testing experiments. In addition, the PULSTAR is equipped with a pneumatic system that can place samples in close proximity to the core to perform neutron activation analysis irradiations. Furthermore, the core is surrounded by 5 beam tubes and has a sixth through beam tube. These beam tubes have been the subject of much development in the past few years resulting in the installation of an advanced neutron imaging facility, a neutron powder diffraction system, an intense positron beam, and an ultracold neutron source. These facilities have resulted in establishing the PULSTAR as a center for fundamental and applied research in neutron physics and the characterization of nanomaterials. Figure 2.2 shows a layout of the PULSTAR bay floor and its various beam tube facilities.

Finally, it should be noted that due to the use of  $UO_2$  fuel and its low enrichment, the PULSTAR reactor is characterized with a negative reactivity feedback behavior, as quantified by its power coefficient of reactivity (PCR), that reaches  $-330$  pcm/MW. This is considered relatively large especially when compared to other common research reactor designs, e.g., MTR reactors, which typically have a PCR that is lower by an order of magnitude or more. Furthermore, the

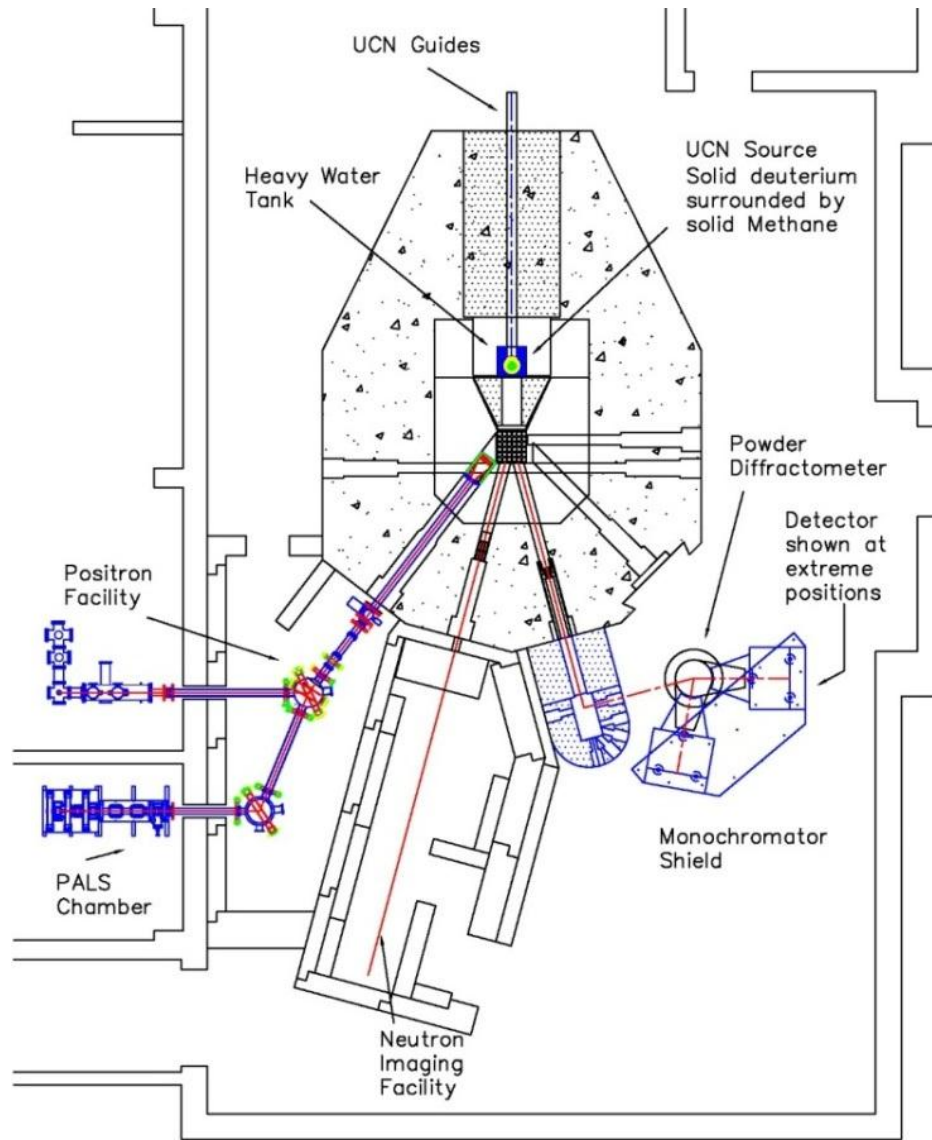


**Fig. 2.2 - A schematic of the PULSTAR bay floor showing various beam tube facilities.**

design of the PULSTAR reactor core represents a highly under moderated system that results in the thermal neutron flux reaching its peak at the periphery of the core and at the entrance of the beam tubes. This results in preferential leaking of thermal neutrons into the beam tubes and in turn enhanced fluxes at the sample positions for the various facilities that are shown in Figure 2.2.

## 2.2 Reactor Power Uprate Project

The upgrade of the PULSTAR systems was executed to allow increasing its power from 1 to 2 MW<sub>th</sub>. This increase in power would directly support its educational and research activities. Fundamentally, the PULSTAR represents an intense radiation (neutron, gamma ray and positron) source. Consequently, doubling its power is expected to result in effectively doubling the available radiation fluxes that are useable in the applications described below. In addition, as a part of the upgrade process, plans are currently underway to allow the refueling of the PULSTAR core with fresh UO<sub>2</sub> fuel assemblies that have identical configuration to the current assemblies (see Figure 2.1) but are enriched to 6% in U-235.

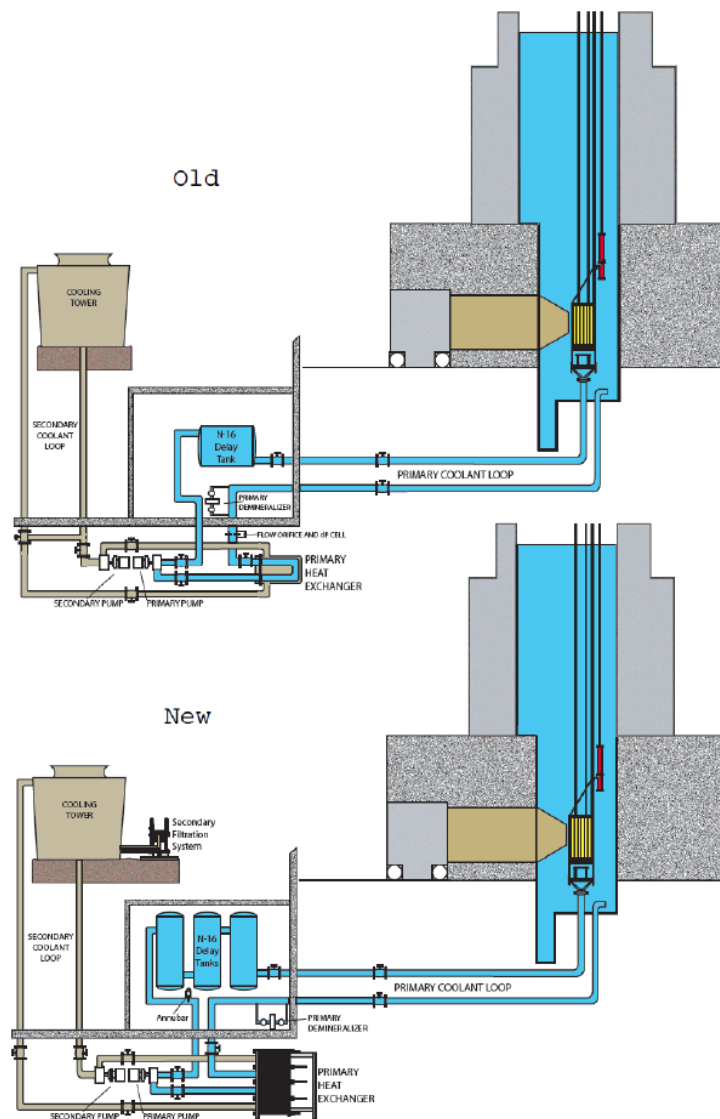


Fig. 2.3 - A schematic of the PULSTAR reactor upgrade of the primary and secondary systems.

In terms of hardware, the upgrade involved a complete refurbishment of the primary and secondary cooling systems for the PULSTAR reactor (see Figure 2.3). This process (and the commissioning of the new systems) was executed during a 4-month shutdown period. In this case, the starting point for the new system design was the preservation of all safety and operational margins that characterized the old system and that comprised its licensing basis as set in the PULSTAR's Safety Analysis Report and its Technical Specifications. Consequently, new primary and secondary pumps (controlled by variable frequency drives), nitrogen ( $N-16$ ) delay tanks (see Figure 2.4), a plate-type heat exchanger, and the supporting valves and coolant flow pipes that are capable of supporting flow rates up to 1000 gallons per minute (vs. the original 500 gallons per minute) were installed. In addition, the original cooling tower was maintained but refurbished to support the increase in power and also equipped with variable speed fan capability and instrumentation, which allows automatic regulation of the fan speed to permit holding the coolant pool inlet temperature at a given set point. This capability allows operating the reactor at its maximum power even on days when the ambient temperature and humidity may approach or reach abnormal highs, which sometimes was not possible under the old system's configuration. The upgrade also included the installation of a secondary system coolant filtration unit, which is expected to reduce the long term maintenance needs and costs.



**Fig. 2.4 –  $^{16}\text{N}$  Delay Tanks in shielding vault**

Upon completion of the systems upgrade process, the commissioning activities for the new system were initiated to perform coolant filling and leak testing, instrument calibrations to support flow and temperature measurements, pump testing and measurement of flow curves, and testing of coolant filtration units. The return of the PULSTAR reactor to operations at the licensed power of 1-MWth was gradually performed by operating at 50%, 90%, 95% and 100% power over a 3-week period. Finally, it should be noted that the installation and commissioning of the new PULSTAR reactor systems was performed following US NRC regulations as prescribed in 10 CFR 50.59 and after approval of the NCSU campus reactor and radiation safety committees.

To support the licensing requirements of the PULSTAR reactor power upgrade, neutronic and thermal-hydraulic analyses of the reactor core and systems have been initiated. The neutronic analysis is performed using the MCNPX code package and is utilized to predict the PULSTAR performance capabilities in a mixed enrichment (4% and 6%) configuration. This includes estimating parameters such as the core's excess reactivity, shutdown margin, reactivity coefficients, and kinetic parameters such as the effective delayed neutron fraction and the prompt neutron lifetime. In addition, the core power distributions are calculated and provided for utilization in the thermal-hydraulic analysis to support predictions of safety performance under steady state and transient operational scenarios. Figure 2.5 shows a layout of the MCNPX model for the PULSTAR core. The validity of the MCNPX model is investigated using PULSTAR data that was measured since the start of its operation in 1972 and to the present day. The measurements include core depletion data, control rod worth information, and power distributions. To date, reasonable agreement has been found between model calculations and the historical data (e.g., see Figure 2.5). Currently, the thermalhydraulic analysis is underway and is utilizing the RELAP5-3D code package. Nonetheless, due to the core power and flow characteristics, it is anticipated that the conservative PULSTAR safety margins, which were predicted during steady state operations and for the potential transient scenarios at 1-MWth, will persist as the power is raised to 2-MWth.

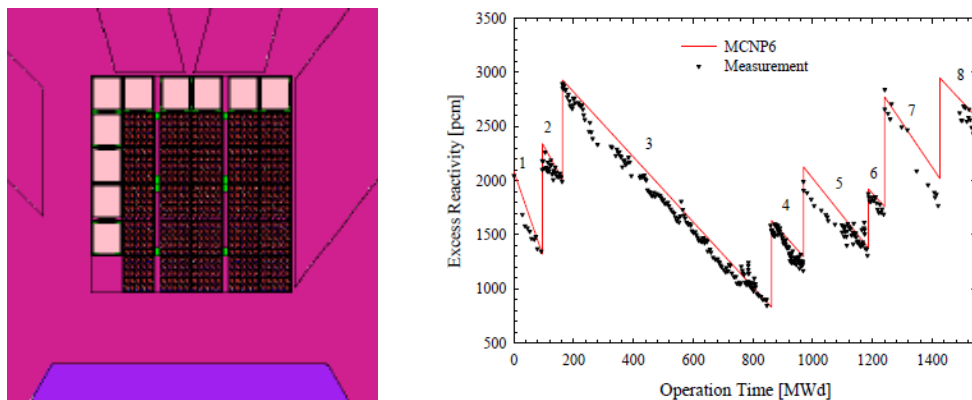


**Fig. 2.5 - The PULSTAR reactor MCNPX core model (left) and the measured vs. predicted core depletion for the period from 1972 to present (right).**

## 2.3 PULSTAR Facility Capabilities

The PULSTAR reactor and supporting laboratories currently offer the following capabilities:

1. Neutron Powder Diffraction Facility (NPDF) and Microstructure Analysis Laboratory
2. Neutron Imaging Facility (NIF)
3. Positron Intense Beam Facility (PIBF) and Defect Analysis Laboratory
4. Ultra-Cold Neutron Source (UCNS)
5. Internet Reactor Laboratory & Training Workshops
6. Neutron Activation Analysis
7. Reactor Irradiations and Isotope Production

There are dedicated facilities for each of the above applications (see Table 2.1 below). The Neutron Diffraction Facility is installed in beamport #4, The Neutron Imaging Facility is installed in beamport #5, the Positron Intense Beam Facility is installed in beamport #6, and the Ultra-Cold Neutron Source, under development, is installed in the reactor “thermal column” region. Internet Reactor Laboratory exercises are hosted from the PULSTAR control room utilizing video-conferencing and online real-time data acquisition systems. In-pool irradiation facilities are utilized for Neutron Activation Analysis, Isotope Production, and other irradiation and instrumentation testing projects. The capabilities of each facility are discussed in detail under Section 3 “User Facility Descriptions” below.

**Table 2.1 - PULSTAR Reactor Facilities / Capabilities**

<u>Facility / Capability</u>	<u>Description / Status</u>	<u>Intensity</u>
Rotating Exposure Ports (4 in-pool, ex-core)	2.5” ID wet sample irradiation terminus.	$1.0 \times 10^{13}$ thermal n/cm <sup>2</sup> /sec $1.0 \times 10^{12}$ fast n/cm <sup>2</sup> /sec
Dry Exposure Ports (2 in-pool, ex-core)	1.25” ID dry sample irradiation terminus.	$4.0 \times 10^{12}$ thermal n/cm <sup>2</sup> /sec $1.0 \times 10^{11}$ fast n/cm <sup>2</sup> /sec
Pneumatic Terminus (1 in-pool, ex-core)	1.25” ID fast rabbit sample transfer system	$1.0 \times 10^{13}$ thermal n/cm <sup>2</sup> /sec $1.0 \times 10^{12}$ fast n/cm <sup>2</sup> /sec
Pool Standpipes (4 in-pool, ex-core)	3.5” ID dry sample irradiation positions	$1.0 \times 10^{11}$ thermal n/cm <sup>2</sup> /sec $5.0 \times 10^9$ fast n/cm <sup>2</sup> /sec
Beamport #1	6-in. diameter radial tube	$1.0 \times 10^{12}$ thermal n/cm <sup>2</sup> /sec at core end
Beamport #2	6-in. diameter tangential ‘through’ tube	$1.0 \times 10^{12}$ thermal n/cm <sup>2</sup> /sec at centerpoint
Beamport #3	8-in. diameter radial tube	$1.0 \times 10^{12}$ thermal n/cm <sup>2</sup> /sec at core end

## NORTH CAROLINA STATE UNIVERSITY

Beamport #4 – Neutron Powder Diffraction Facility (NPDF)	6-in. diameter radial tube; NDF facility installed.	$\sim 0.5 \times 10^5$ 1.4 Å n/cm <sup>2</sup> /sec on target
Beamport #5 – Neutron Imaging Facility (NIF)	6-in. diameter radial tube; NIF facility installed.	$\sim 5.0 \times 10^6$ thermal n/cm <sup>2</sup> /sec at 6.5 meter imaging plane.
Beamport #6 – Positron Intense Beam Facility (PIBF)	12 in. by 12 in. sq. radial tube; IPS moderator assembly and beam transport system installed.	$6 \times 10^8$ positrons/second at target; beam spot diameter is 25 mm; e+ energy variable up to 30 keV
Thermal Column – Ultra-Cold Neutron Source (UCN)	5'x5'x7' cavity in biologic shield adjacent to reactor core. Cryogenic plant installed.	Projected intensity of 6 to 16 million UCN's per second.
PULSTAR Internet Reactor Laboratory	Video conferencing system (Polycom VS4000) located in PULSTAR control room with remote operation of cameras directed at console instruments. Online reactor experiment data acquisition system.	

### 3. User Facility Descriptions:

#### 3.1 Neutron Powder Diffraction Facility and Microstructure Analysis Laboratory

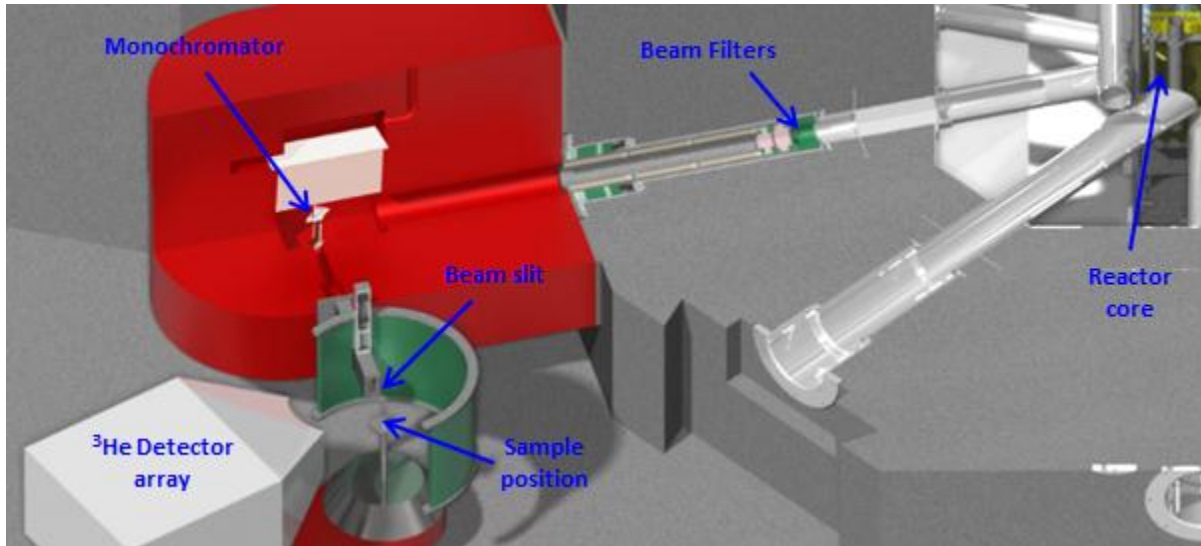


**Fig. 3.1.1 – Neutron Powder Diffraction Facility**

The Neutron Powder Diffraction Facility and Microstructure Analysis Laboratory utilize the capabilities of the double-axis neutron diffraction system (see Figure 3.1.1) installed at beamport #4 of the PULSTAR reactor. The NPDF is a sensitive instrument that compares very favorably with existing diffraction instruments at other neutron beam laboratories. When combined with the function of the Oscillating Rotating Collimator (ORC), the facility is capable of analyzing samples under high-temperature or cryogenic conditions.

#### **Neutron Scattering for the Characterization of Bulk Materials**

The physical properties of the neutron enable its application as a powerful nondestructive probe for bulk materials characterization. Neutron powder diffraction is complementary to other materials characterization methods, such as X-ray diffraction, with the following advantages:

- Neutron scattering length is not dependent on atomic number (see Figure 3.1.2). It is possible to observe the light atoms, such as H, Li, and distinguish the adjacent elements in the periodic table.
- Neutron scattering length is isotope dependent. Isotopic substitution can be used to study crystalline structures which contain high neutron absorbing elements, such as B, Gd, Cd, Sm, etc...

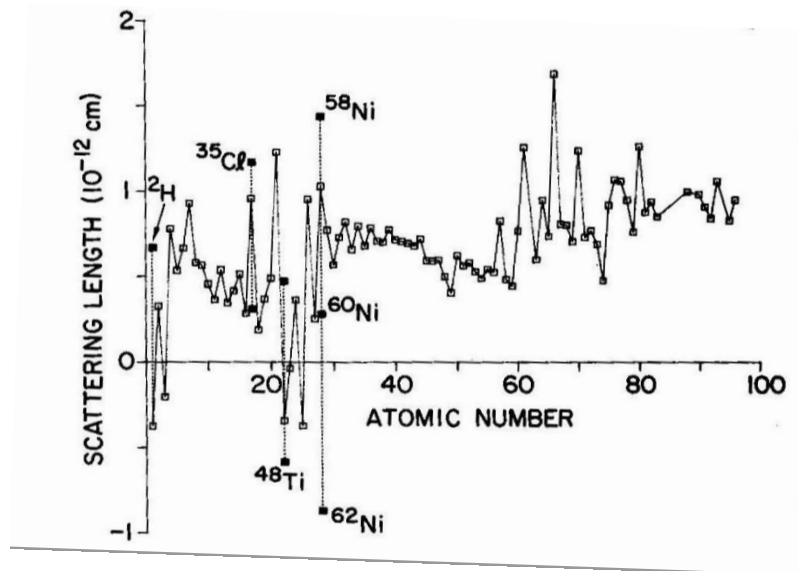


**Fig. 3.1.2: The bound-atom scattering length for different elements. Values are shown for naturally abundant isotopic compositions. The solid squares indicate values for isotopes often used in isotope-substitution experiments (e.g.  $^2\text{H}$ ,  $^{35}\text{Cl}$ ,  $^{48}\text{Ti}$ ,  $^{58/60/62}\text{Ni}$ ).**

- Neutrons are scattered by the nuclei (except for magnetic scattering), thus the form factor is flat. It is good for studying phenomena requiring data over a large range of interplanar spaces; for example, isotropic and anisotropic displacement parameters.
- Neutrons are usually deeply penetrating so they can diffract from specimens contained within a cryo-refrigerator or furnace.
- Neutron diffraction can be used to study magnetic structures.

When a polycrystalline specimen is bathed in a monochromatic (single wavelength) beam of neutrons, there are always many grains of the sample that are aligned to reflect the radiation according to Bragg's Law (Figure 3.1.3). The diffracted neutrons form cones of radiation corresponding to the many different atom plane spacings ( $d$ ) in the crystals. If a detector is arranged to scan through the scattered radiation, a series of peaks appears as a function of angle. The positions of the peaks (in angle) are determined by the space group and the unit cell parameters. The intensity of the diffraction peaks is controlled by the structure factor which is dependent on the arrangement of atoms in the unit cell (the fundamental crystal building block). Using a technique called Rietveld Refinement, the observed diffraction pattern can be compared with the pattern calculated from the model of the crystal structure. A good agreement between the observed and calculated patterns can be achieved by adjusting the parameters of the model of crystal structure, such as the lattice parameters, atomic positions and occupancies, and the thermal displacements. The result is the "refined" crystal structure for the specimen.

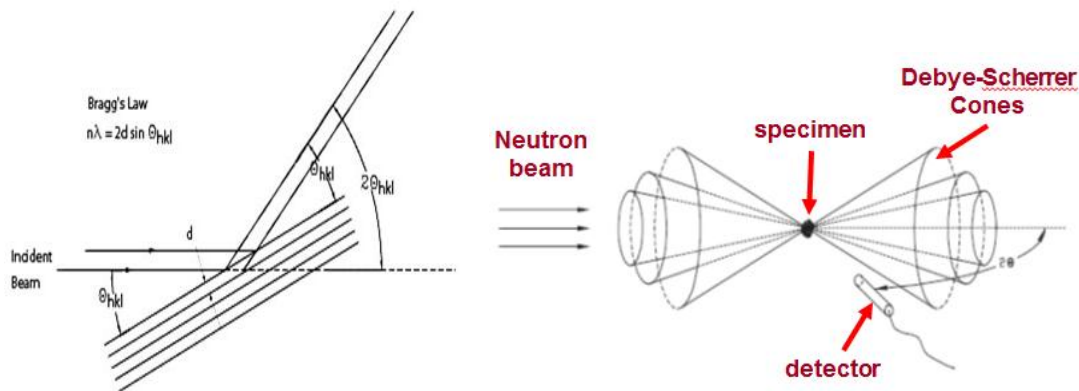


**Fig. 3.1.3: Bragg diffraction and Debye-Scherrer cones for Bragg scattering from a crystalline powder**

Neutron diffraction data can be directly compared to theoretical models of crystal structure and composition, opening a wide variety of possible applications, such as:

- ❑ New material crystal structure and composition: In the development of new materials, the correlation of structure, synthesis conditions and properties is essential.
- ❑ Alloy atom location: The intensity of diffraction peaks is directly related to the atom species and fractional occupation of the crystal atom sites.
- ❑ Solid – Solid phase transformation: Many materials change their crystal structure in response to changes in their environment (temperature and pressure). New crystal phases result in new diffraction peaks – the unmistakable signature of phase transformation.
- ❑ Chemical and solid-state reaction pathways and kinetics: Many chemical and solid-state reactions can be monitored quantitatively through the intensity of the diffraction peaks corresponding to the various components.
- ❑ Material stress – strain analysis: When crystalline materials are put under stress, the spacing between their atomic planes is changed. This results in a shift of the diffraction line positions. With neutron diffraction it is possible to probe material stress distributions in real engineering materials.
- ❑ Magnetic ordering and magnetic structure determination.

**Application Case Study – Structure of Irradiated Nuclear Grade Graphite**

Nuclear graphite specimens were studied using the NPDF. One was un-irradiated (NBG-10), and the other (L25) was irradiated at 280 °C with total fast neutron fluence of  $4.9 \times 10^{25}$  n/m<sup>2</sup>. Table 3.1.1 summarizes the results of the analysis comparing the irradiated and un-irradiated samples. Figure 3.1.4 details the diffraction patterns obtained. Further

information concerning this analysis may be found in Appendix A – *Analysis of Nuclear Graphite using the NPDF and Microstructure Analysis Laboratory.*

**Table 3.1.1: Results for the analysis of the un-irradiated and irradiated graphite samples.**

Parameters	NBG-10 (un-irradiated)	L25 (irradiated at 280 °C)
$d_{002}$ (Å)	3.3677(1)	3.462(1)
$a$ (Å)	2.4598	2.4069(9)
$P$	0.4412(16)	1.0*
$P_t$	0.1340(17)	
$1-P-P_t$	0.4248	0.0
$\langle \delta^2 \rangle$ (Å <sup>2</sup> )	0.0109(1)	0.31(2)
$G$		0.40(2)
$Z$		0.0661(8)
$M$	70(2)	8.3(3)
$La$ (Å)	539(19)	42.45(8)
$P_0$	0.0*	0.0*
$B$ (Å <sup>2</sup> )	0.700(6)	1.28(5)
$\chi^2$	3.5	1.8

\* fixed in refinement.

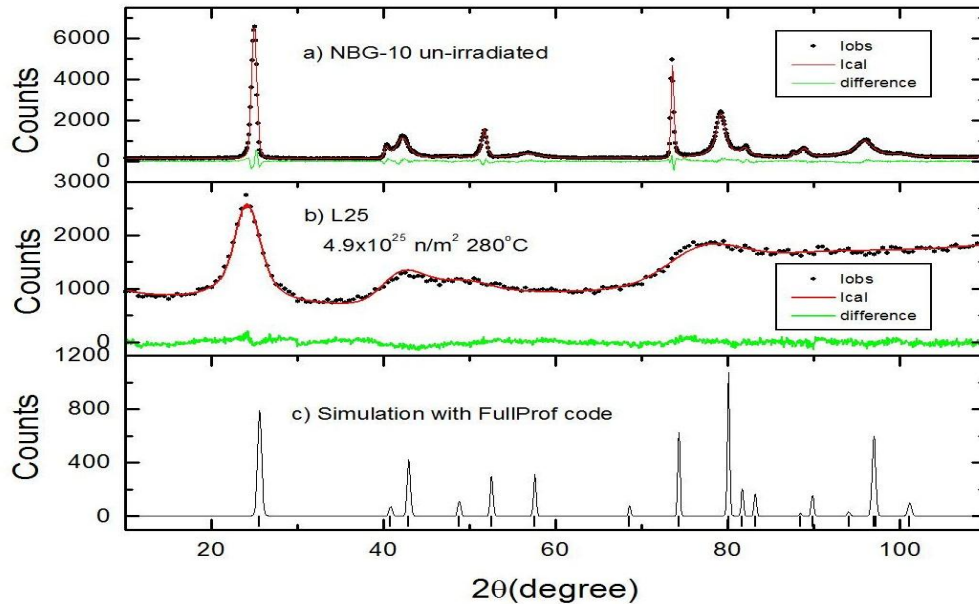


**Fig. 3.1.4: The neutron diffraction patterns of reactor grade graphite specimens. a) NBG-10 unirradiated graphite, b) L25 irradiated graphite, and c) pattern simulated with FullProf program. The black points are the observed data, the red line is the calculated data, and the green line is the difference of observed and calculated data.**

**NPDF Instrument Characteristics**

The thermal neutron flux entering the beamport is  $\sim 3 \times 10^{12}$  n/cm<sup>2</sup>/s. Given that the instrument utilizes a radial beamport directly facing the reactor core, a six-inch thickness single crystal sapphire filter is employed as a fast neutron filter and high energy gamma radiation shield. A bent, perfect single crystal silicon, doubly focusing monochromator extracts a 1.479 Å (511) or a 1.762 Å (331) neutron beam perpendicular to the main beam. Table 3.1.2 summarizes the parameters associated with the NPDF instrument.

**Table 3.1.2 – NPDF Parameters**

Beam Spectrum:	$\sim 3 \times 10^{12}$ Thermal n/cm <sup>2</sup> /s at source; $\sim 0.64 \times 10^5$ 1.479Å n/cm <sup>2</sup> /s on sample
Monochromator:	Bent silicon single crystal
Take off angle:	$2\theta_m = 90^\circ$
Wavelength:	1.479Å (511), 1.762Å (331)
Scattering angles:	$5^\circ \leq 2\theta \leq 125^\circ$
Detector bank:	15 <sup>3</sup> He detectors
Beam size at sample position:	7cm x 1cm
Minimum resolution ( $\Delta d/d$ ):	$2.91 \times 10^{-3}$ (Ø3mm holder), $3.34 \times 10^{-3}$ (Ø5mm holder)

The monochromator consists 9 silicon single crystal blades which are bent horizontally to a radius of 12.25m. The vertical focusing is accomplished by mounting the blades with polygonal approximation to a radius of 1.44m. The wavelength is 1.479Å (511) and 1.762Å (311). The monochromator and its double focusing features are shown in Figure 3.1.5 (a), (b) and (c).

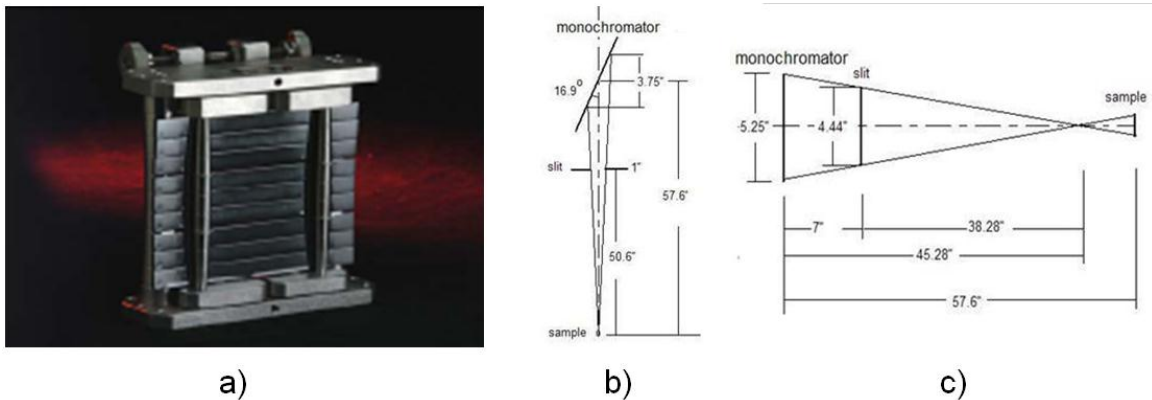


**Fig. 3.1.5 – Monochromator (a); Neutron focusing in horizontal (b) and vertical (c) planes.**

To reduce background in the detector from scattering occurring outside of the sample volume, an Oscillating Radial Collimator (ORC) is utilized with blades focused to the sample position (see Figure 3.1.6). The blades are coated with GdO powder, which strongly absorbs thermal neutrons. The neutrons scattered at the sample position can pass through the collimator, but the neutrons scattered at other positions will be stopped. The oscillating movement averages the shade of the blades and results in a smooth background. The ORC enables the installation of a sample chamber providing a low or high temperature environment for sample testing. Neutrons scattered in the sample chamber wall are blocked by the ORC to prevent noise in the detector array.

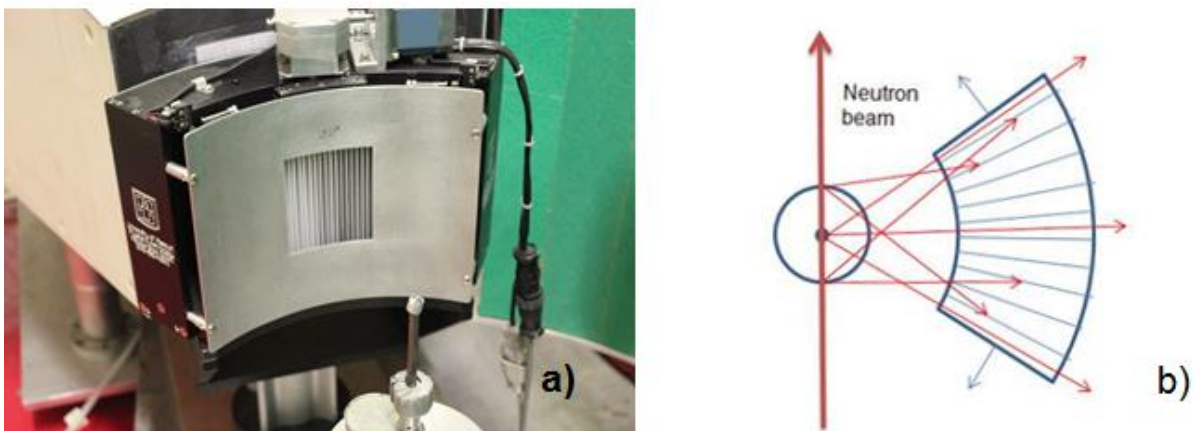


Fig. 3.1.6 – (a) ORC, and (b) function of the ORC

The position sensitive detectors are  $^3\text{He}$  proportional counters which have an active length of 24 inches, a diameter of 1 inch, and are filled with 8 Atm of  $^3\text{He}$  and 4 Atm of Argon. Neutron detection is through the reaction:  $n + ^3\text{He} \rightarrow ^1\text{H} + ^3\text{H} + 768\text{keV}$ . The event position can be found by comparing the charges collected at the ends of each detector, and the event positions can be transformed to the  $2\theta$  angle. The detector has about 3mm resolution and can collect 400 points of data at one position. 15 detectors are stacked in vertical direction (see Fig. 3.1.4) which gives a 15 inch vertical acceptance. The detector array is attached to a moveable cassette and can be moved from  $15^\circ$  to  $115^\circ$  to cover the entire scattering angle  $5^\circ$  to  $125^\circ$ . A fission chamber located at the beam before the sample is employed as the monitor. The detectors collect data at each section for a fixed monitor count to ensure the incoming neutron at sample position is same for each section.

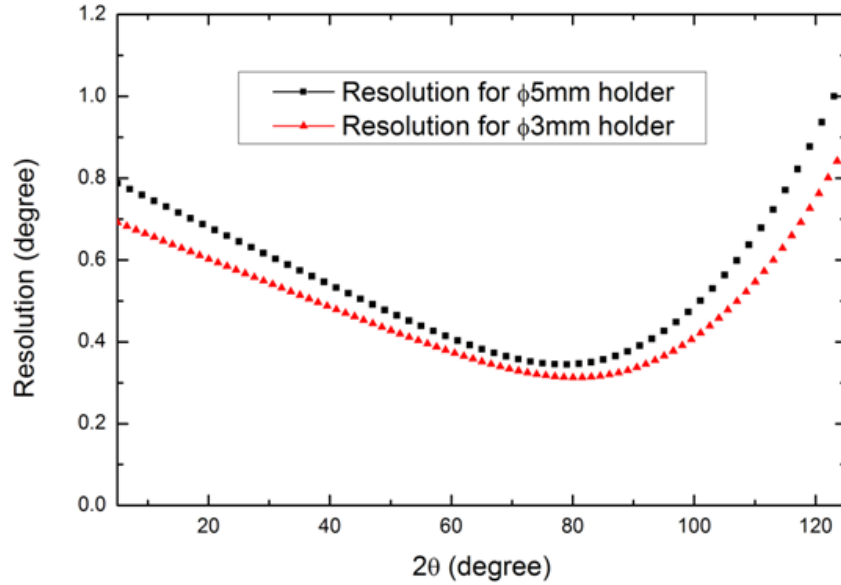


Fig. 3.1.7: Resolution of Instrument with Ø3mm and Ø5mm holder

The NPDF is optimized for analysis of small volume specimens typically employing a Ø5 mm x 64 mm sample container and about 1.2 cm<sup>3</sup> of specimen. The intensity and resolution of the NPDF instrument compare very favorably with existing instruments at other neutron beam laboratories (see Figure 3.1.7 and Table 3.1.2).

Table 3.1.2 – Intensity Comparison

Facility	Power (MW)	Flux (n/cm <sup>2</sup> s)	Sample Size (cm <sup>3</sup> )	Flux at sample (n/cm <sup>2</sup> s)
NIST BT-1 Cu-311/15'	20	4x10 <sup>14</sup>	10	4x10 <sup>5</sup>
NIST BT-1 Cu-311/7'	20	6x10 <sup>14</sup>	10	2x10 <sup>5</sup>
MURR PSD-II	10	6x10 <sup>13</sup>	0.35-1.5	1.35x10 <sup>5</sup>
NCSU	1	2.7x10 <sup>12</sup>	0.35-1.5	0.64x10 <sup>5</sup>

### 3.2 Neutron Imaging Facility

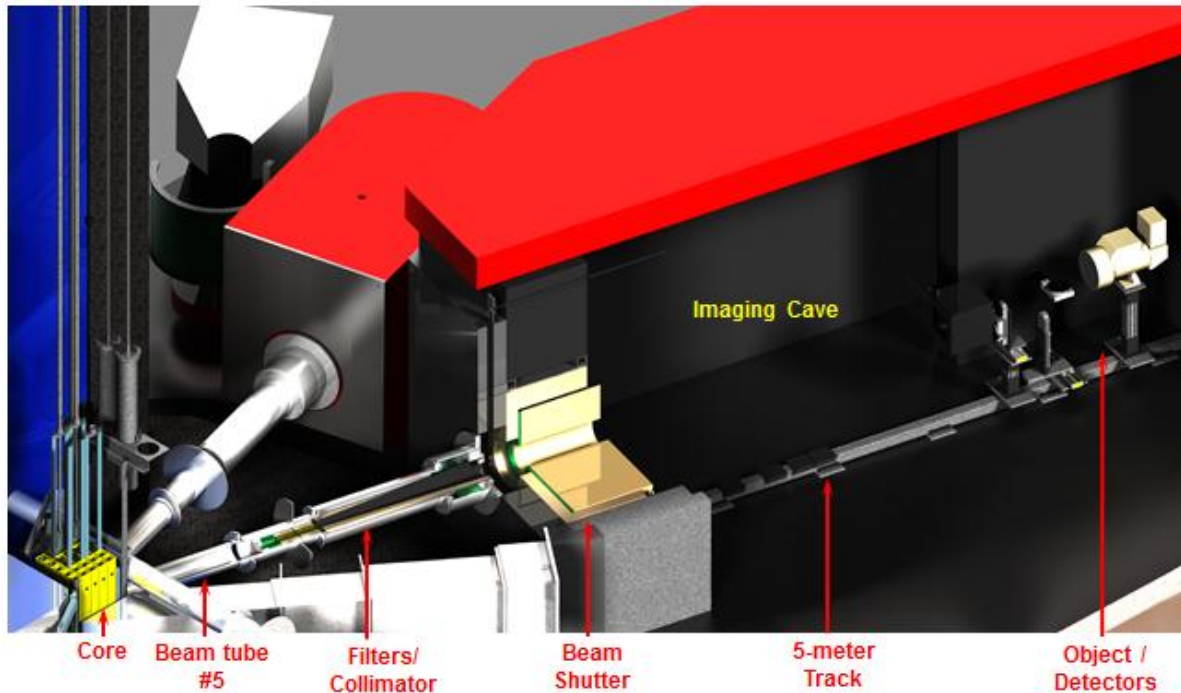


Fig. 3.2.1 – Neutron Imaging Facility

The Neutron Imaging Facility (NIF) is located in beam port #5 of the PULSTAR Reactor (see Figure 3.2.1) and provides a powerful non-destructive imaging technique for the internal evaluation of materials or components. Neutron radiography involves the attenuation of a neutron beam by an object to be radiographed, and registration of the attenuation process (as an image) digitally or on film. It is similar in principle to X-ray radiography, and is complimentary in the nature of information supplied. The interactions of X-rays and neutrons with matter are fundamentally different, however, forming the basis of many unique applications using neutrons. While X-rays interact with the electron cloud surrounding the nucleus of an atom, neutrons interact with the nucleus itself.

#### Neutron Imaging

Neutron imaging requires a collimated neutron source, an object of radiographic interest, and detection system to record the image (see Figure 3.2.2). Thermal neutrons are preferred for imaging purpose. To form a usable beam, a collimation system is used to select neutrons in an essentially parallel direction and direct them onto the object. The most common collimator design is a divergent collimator with a small entrance aperture and a larger exit. The spread of the beam is dependent upon the ratio of the collimator length ( $L$ ) to the aperture size ( $D$ ), referred to as the  $L/D$  ratio. This ratio is a characteristic

parameter of each collimator. A higher  $L/D$  results in a sharper beam at the expense of a lower neutron flux. The material or object to be radiographed is placed in the collimated beam. The neutrons are attenuated by elements in the object with high thermal neutron attenuation coefficients as the beam passes through. The intensities and locations of the neutrons remaining in the beam are then collected by detection systems. The result is a negative image of the object, with the light areas indicating the greatest neutron attenuation by the object, and the dark areas indicating the least neutron attenuation.

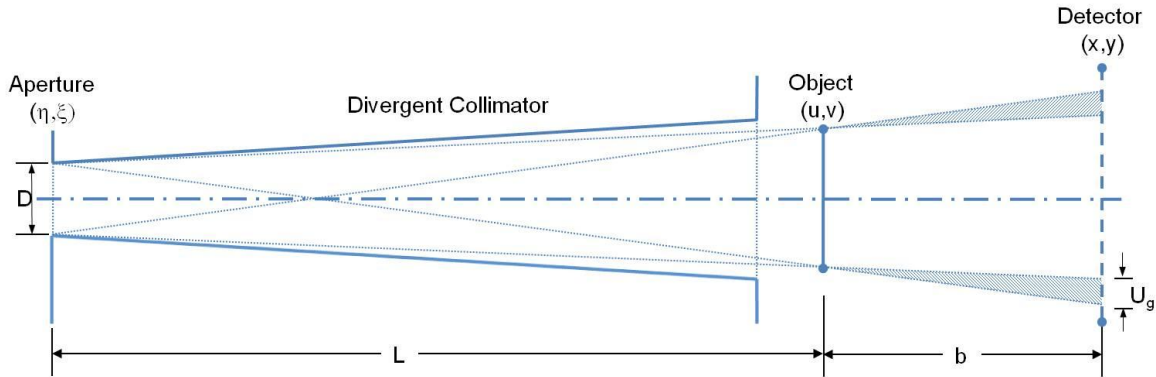


Fig. 3.2.2: Configuration of a neutron imaging system

### NIF Instrument Characteristics

Beamport #5 of the PULSTAR provides the NIF with a nominal source flux of  $2.5 \times 10^{12}$  n/cm<sup>2</sup>/sec at 1 MW. The beam is collimated and filtered with 12 inches of single crystal sapphire. The current aperture is a 1.57"×1.57" (1.7" effective diameter) square cross section opening in a BORAL plate, which yields an  $L/D$  ratio of  $\sim 150$  at the 6.5 meter imaging plane. The resolution of the system is  $\sim 33 \mu\text{m}$  for conventional radiographic film. Measurements using ASTM standards show that the NIF achieves a beam quality classification of  $I^A$ . Table 3.2.1 summarizes parameters associated with the NIF.

Table 3.2.1 – NIF Characteristics

Parameter	Value
Neutron Flux	$3.2 \times 10^6$ to $3.7 \times 10^7$ n/cm <sup>2</sup> /sec
TNC	$\sim 70\%$
N/G	$4.43 \times 10^4$ to $1.34 \times 10^6$ cm <sup>-2</sup> mR <sup>-1</sup>
L/D	100 to 150
Divergence	$\sim 2.29^\circ$
Cd Ratio	$\sim 450$
Scatter Content	$\sim 1.8\%$

Imaging techniques available include conventional film, molecular phosphor digital imaging plates, Thompson Tube imaging systems and real-time imaging system using CCD camera with Micro-Channel Plate or ZnS scintillator. Neutron tomographic measurement may be made utilizing a motorized sample positioning system in concert with real-time imaging systems.

### Neutron Imaging Applications:

Examples of Neutron Imaging applications performed at NCSU include:

- Coolant channel blockage in turbine blade castings (see Figure 3.2.2).
- Water transport in operating PEM Fuel cell (see Figure 3.2.3).
- Plant root growth in soil plaques (*in-situ*).
- Water penetration in concrete.
- Spray pattern from fuel injector nozzle.

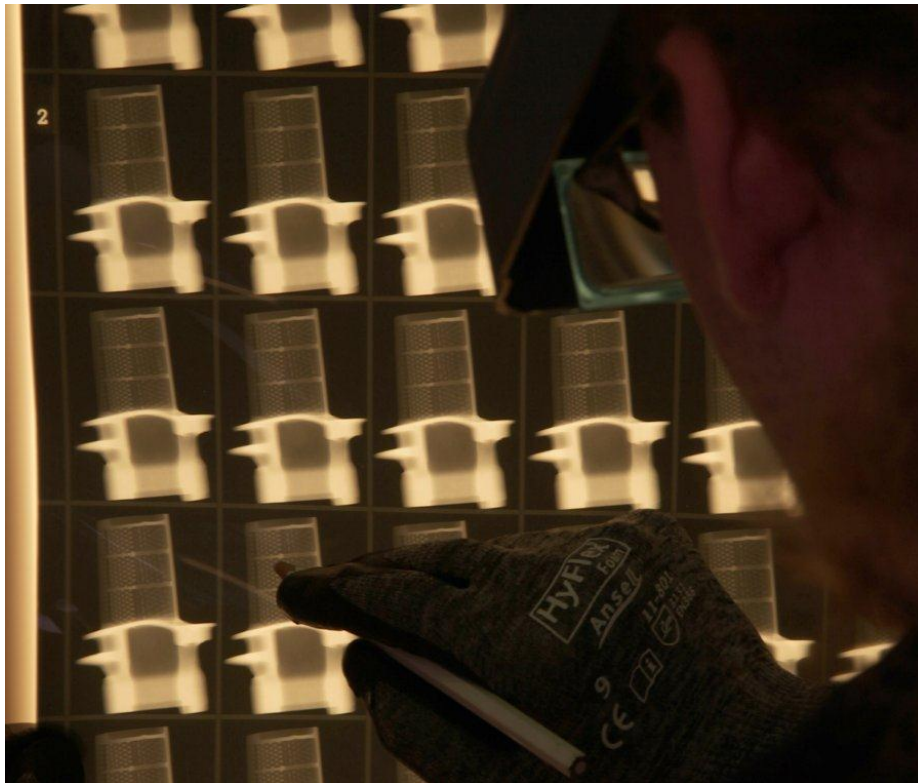


**Fig. 3.2.2 – Turbine Blade Castings (single emulsion x-ray film)**

Additional applications could include:

- Defects in silicon nitride (Si<sub>3</sub>N<sub>4</sub>) ceramics.
- Imaging A/C refrigeration components for behavior of lubricating & cooling oils.
- Detection of corrosion and entrapped moisture in mechanical structures.
- Studying disbonding of carbon fiber composites (CFC's).

- Measuring boron concentrations in shielding materials.
- Measuring effectiveness of moisture repelling agents in building materials.
- Imaging shock waves in gases.
- Analysis of distribution of electrotransported hydrogen in palladium.
- Quantitative evaluation of nuclear fuel pin structural features.
- Imaging of wetting front instabilities in porous media.

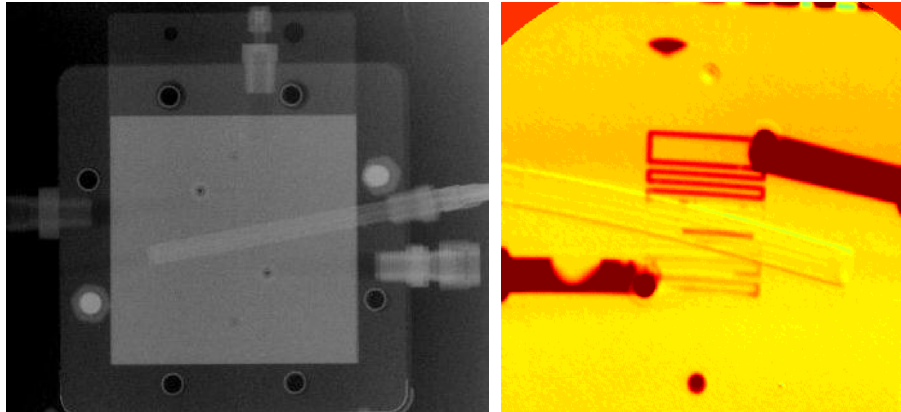


Fig. 3.2.3 –PEM Fuel Cell: dry (at left using molecular phosphor), and operating (at right using Thompson Tube camera)

### Enhanced Imaging Techniques

#### 1. Coded Source Imaging

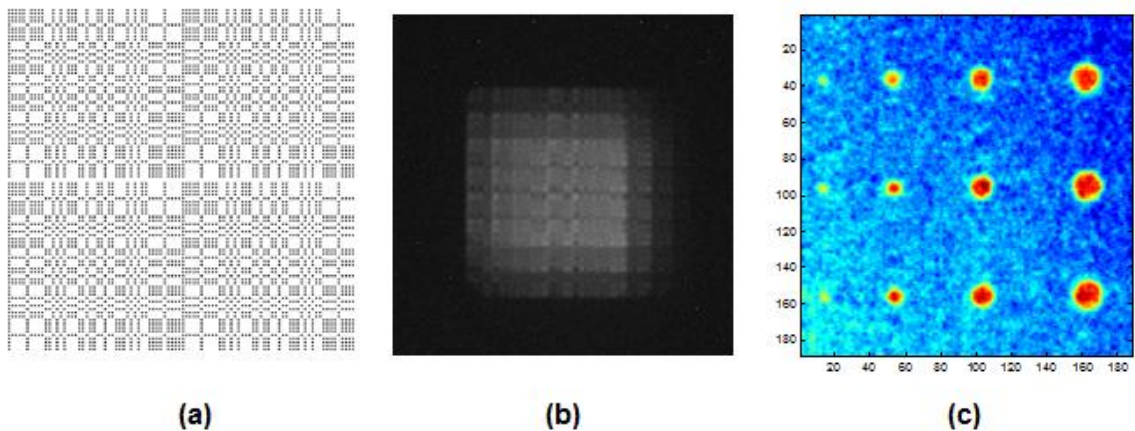


Fig. 3.2.3 – Coded Source Imaging: (a) The Design of a 94×94 MURA mask. 4416 Pinholes with diameter of 200  $\mu\text{m}$  are distributed on a grid with spacing of 400 $\mu\text{m}$ . A mask based on the design has been made on a 450 $\mu\text{m}$ -thick Gd foil and measurements have been performed imaging testing phantoms that were also made on Gd foils. (b) is a recorded image of multiple pinholes as the object, at magnification of 3. The reconstructed result (c) reflects the distribution of the object holes, the diameters of which vary from 200 $\mu\text{m}$  to 800 $\mu\text{m}$ .

Coded source imaging is used to obtain high neutron flux (intensity) and high image resolution at the same time. To achieve this, the neutron source is encoded by a mosaic of pinholes. The collection of pinholes is known as the aperture or mask (see Figure 3.2.3). The mask pattern should be wisely chosen, so that a corresponding decoding array exists and gives a delta function when correlating with the mask. A large number of pinholes are used to ensure a sufficient single-to-noise ratio in the image. Each pinhole will deposit a shadow of the object at the detector. The objects are placed away from the detector, and the reconstruction provides a magnified image of the objects. The recorded image can be expressed as a convolution between the distribution of the mask and the distribution of neutron-attenuation in the object. By correlating the recorded image with the decoding array, the distribution of the object can be extracted, without greatly amplifying the noise. The system resolution will not be limited by resolution of the detector.

## 2. Phase Contrast Imaging

Non-interferometric phase contrast neutron imaging is a technique utilized to increase the spatial and contrast resolution of neutron radiographs (see Figure 3.2.4). Phase contrast formation in the image, especially at edges, is enhanced due to phase shifts that take place as the neutron wave passes through regions in the sample that differ in the coherent scattering length density.

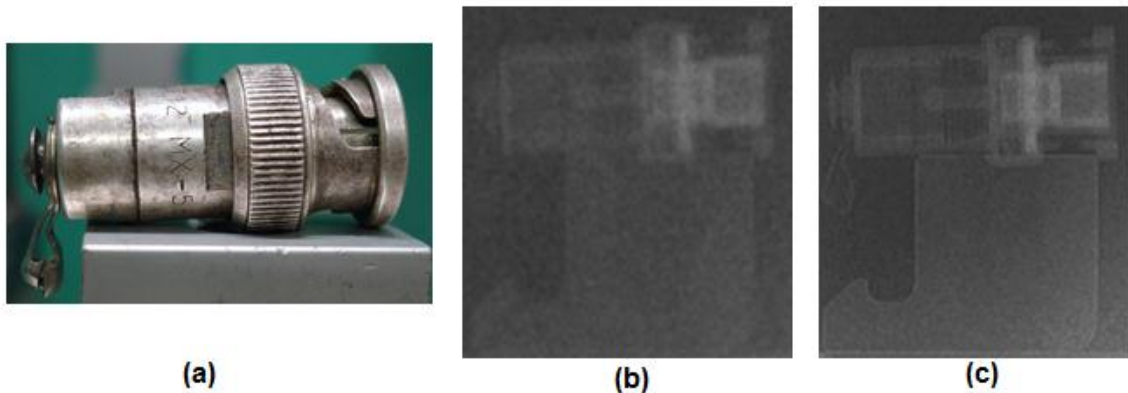


Fig. 3.2.4 (a) The photograph of the BNC connector used as a sample for phase contrast neutron imaging. The image of the BNC connector taken using Fuji BAS-NDG image plate (b) at  $R = 2.5\text{cm}$  (c) at  $R = 250\text{cm}$ . The exposure time for both the images was 45 minutes at 1MW reactor power.

## 3. Neutron Tomography

Similar to medical “Cat Scan” and Magnetic Resonance Imaging, neutron tomography creates a three dimensional image of a sample by reconstructing a series of 2D

radiographs taken as the sample is rotated in the neutron beam. Neutron tomography allows the visualization of the inner structure of a sample of interest.

The NIF uses a Cross positioning system to accurately move and rotate an object with +/- 16  $\mu\text{m}$  linear and +/-2.73 arc sec rotational accuracy. The imaging system components utilized for tomography are detailed in Table 3.2.2 below.

**Table 3.2.2 – Imaging Camera Characteristics**

Camera	Andor iKon L-936
Active pixels	2048x2048
Sensor size	27.6x27.6 mm
Pixel size (WxH)	13.5 $\mu\text{m}$ x13.5 $\mu\text{m}$
Maximum readout rate	5 MHz
Lenses	Micro-Nikkor f/2.8 55mm
Camera box structure	Anodized aluminum
Scintillator screen	LiF/ZnS 0.45 mm & 0.25 mm thick
Mirror	Front surface soda-lime glass
Reconstruction Software	Octopus

### 3.3 Positron Intense Beam Facility (PIBF) and Defect Analysis Laboratory

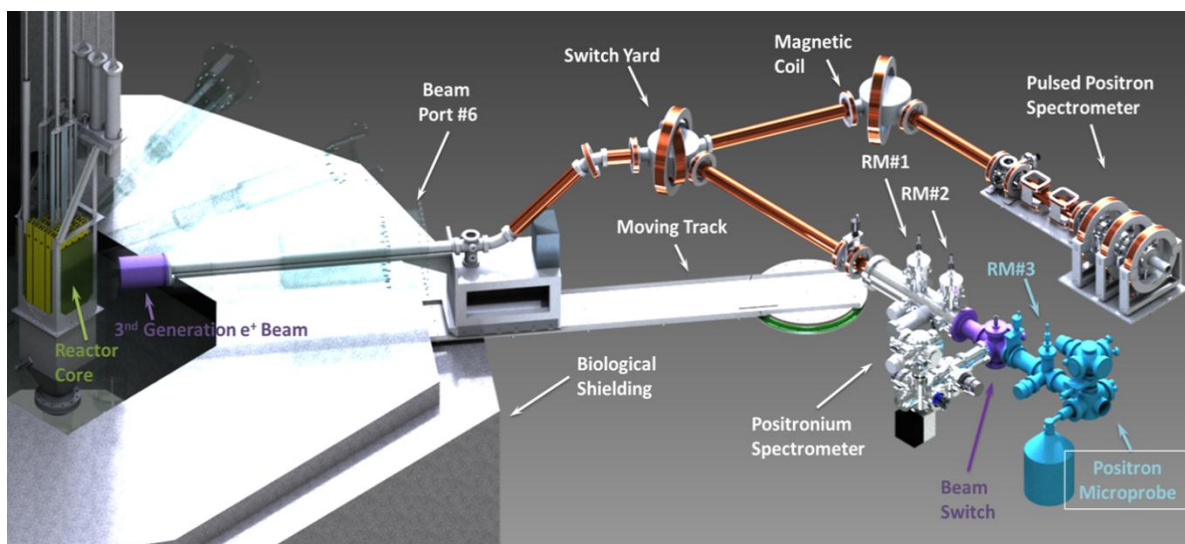


**Fig. 3.3.1 - A schematic drawing of the Positron Intense Beam Facility**

The Positron Intense Beam Facility (PIBF) includes an Intense Positron Source (IPS) installed in beamport #6 of the PULSTAR Reactor, a Pulsed Positron Annihilation Spectrometer (e<sup>+</sup>-PAS), and a Positronium Positron Annihilation Spectrometer (Ps-PAS), as shown in Figure 3.3.1 above. The physical properties of the positron enables its application as a unique and nondestructive probe for materials characterization, especially the detection of the atomic-level open spaces, e.g. vacancies, free volumes, and voids, in condensed matter. More specifically, the positron annihilation events are measured in the time and energy domains by positron annihilation lifetime spectroscopy (PALS) and Doppler broadening spectroscopy (DBS) to obtain information directly related to the properties of these open spaces. Examples of these measurements include depth-profiled PAS on inhomogeneous vacancy, pore structure, and morphology that are intrinsic to materials, such as polymers, nanocomposites, thin films, membranes, and/or introduced by specific procedures. Additionally, *in-situ* measurement using the positron as a probe during thermal, mechanical, electrical, and adsorption processes is another major advantage of the PAS techniques.

#### **Positron Annihilation Spectroscopies; PALS and DBS**

The positron – the antimatter of the electron – has been used as a probe to study the defect properties of materials for several decades. Due to its positive charge, positrons can naturally diffuse to and be trapped in vacancies and open spaces of materials before they finally annihilate with electrons, and emit photons with total energy of 1.022 MeV – a complete conversion of mass to energy following Einstein’s famous equation,  $E=mc^2$ . From the specific information in the energy and time domains of the e<sup>+</sup>-e<sup>-</sup> annihilation photons,

characteristics of vacancy and defect can be extracted of the target materials. Positron annihilation spectroscopies are non-destructive, quantitative with unique sensitivities, and complementary to traditional intrusive and microscopic techniques. Additionally, instead of using positrons emitted from radioactive sources with broad energy distributions, by generating a mono-energetic positron beam, one can control the penetrating power of the positrons and examine depth dependent effects in thin films.

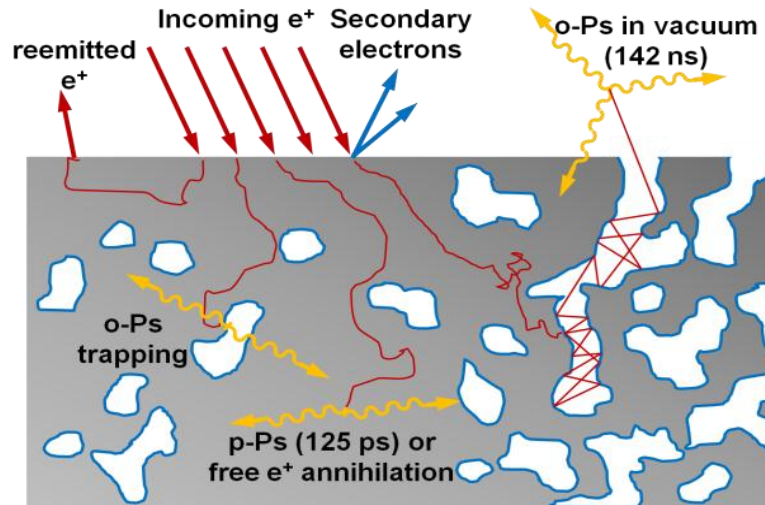


**Fig. 3.3.2 - Positron and Positronium Interactions with Condensed Matter**

Positron Annihilation Lifetime Spectroscopy (PALS) measures the decay lifetime of positrons upon their first injection into the materials of interest. Immediately after their implantation, the positrons lose most of their kinetic energy by scattering with the host atoms and thermalize rapidly. The following diffusion process may result in the trapping of the positrons in defects and voids before their eventual annihilation with the environmental electrons (see Figure 3.3.2). The positron annihilation lifetime is directly related to the electron density, which is sensitive to the concentration and type of vacancy defect and defect clusters.

In semiconductors and insulators, positrons can also form positronium, a meta-stable bound state of a positron and an electron. The lifetime of the positronium triplet state (spin of 1), also called ortho-positronium, is found to be directly related to the size of the voids where it annihilates, and is not sensitive to the material itself (see Figure 3.3.3). This unique feature has found a wide variety of applications in characterizing nano-voids and free volumes in polymers and thin films. Therefore, PALS can also refer to positronium annihilation lifetime spectroscopy.

Another positron spectroscopic technique, Doppler Broadening Spectroscopy (DBS) of the annihilation irradiation, examines the energy spread of the 511 keV back-to-back

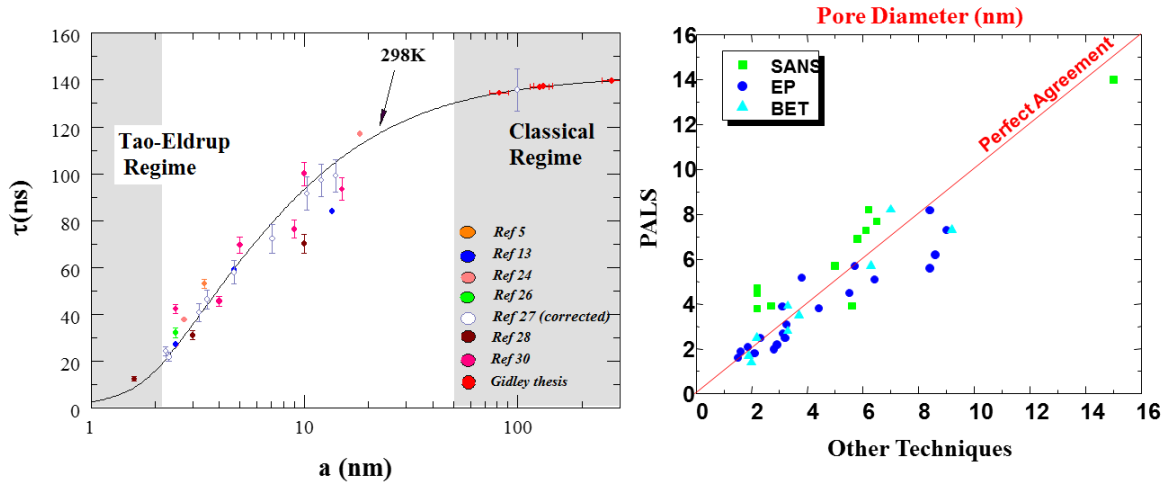


**Fig. 3.3.3 – Pore size calibration of Ps lifetime with Tao-Eldrup model and round-robin comparisons with other techniques**

annihilation gamma due to the momentum of the annihilating electron when the annihilation occurs. Since the electron energy levels vary in the vicinity of ion cores and vacancies, DBS provides complementary information of the vacancy type and density in the energy domain.

Traditional PALS and DBS directly using  $^{22}\text{Na}$  as a typical positron source, which emits high energy positrons with a wide energy spread, and is only suitable for studying thick (millimeter range) materials. The advent of mono-energetic positron beams with controllable positron implantation depth (see Figure 3.3.4) enabled the study of thin films, surfaces, interfaces, and other depth-dependent localized/heterogeneous properties. In particular, beam-based positron spectroscopies have demonstrated extensive utility in characterizing very thin films (tens to hundreds of nanometers) on thick substrates.

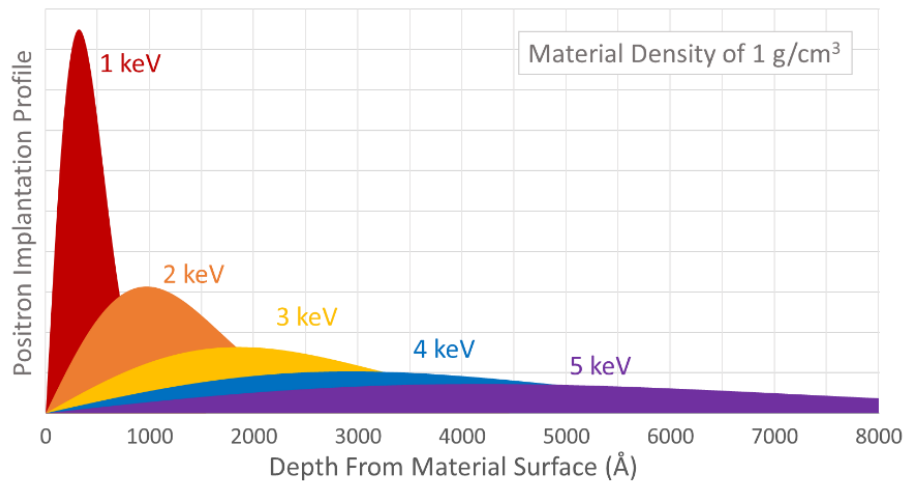


**Fig. 3.3.4 - Positron implantation profile at different beam energies assuming a film density of 1.0 g/cm<sup>3</sup>.**

Intense positron sources (IPS), like the one at the NCSU PULSTAR reactor, would tremendously facilitate the use of PALS and DBS techniques in materials defect/vacancy characterizations, especially in data extensive and/or time restraining situations.

**Materials Characterization Applications**

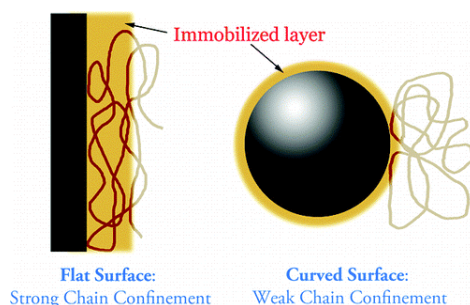
Embraced by the microelectronics industry as a standard characterization technique for low-*k* dielectrics, positron annihilation spectroscopy technique is sensitive to both the size and concentration of voids in solids and has found applications in the analysis of **vacancies**, **nano-voids**, and **morphology** of materials ranging from **metals**, **semiconductors** to **insulators** and **composites**. As an example of its application, PALS has been used to study the vacancy and vacancy clusters in nuclear graphite and, the *Characterization of Defects in Nuclear Graphite Using the PIBF and Defect Analysis Laboratory* is included in Appendix B.



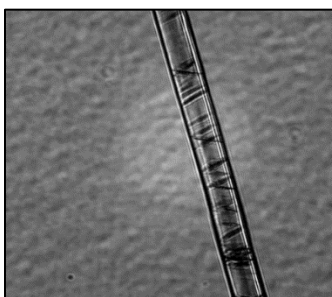
PAS can address important questions in a variety of polymers, such as PEMs and OPVs for energy applications, where free volumes play critical roles. For example, organic semiconductors are promising candidates for low-cost, flexible electronics that can be deposited by a simple printing process. The nanostructure of the OPV materials is believed to have profound impact on the final device performance. However, their exact correlation is still topics of debate. Since PALS is

sensitive to the intermolecular packing, it could provide a straightforward and quantitative view on this matter and may even lead to a rapid route to predict the performance of organic semiconductors.

The application of PAS can also be extended to any two phase system where the interfacial behavior is interested, such as polymer nanocomposite, semicrystalline materials and highly porous materials. In some of these systems the electrical, chemical, and mechanical properties at the interface is crucial in determining the final performance of these systems. In model systems that are carefully made, PALS can be



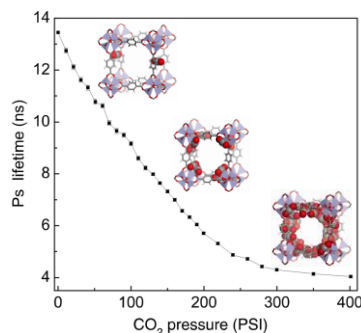
very useful in characterizing the confinement effect and even drawing critical correlation about the interfacial properties between thin films and nanocomposite. This can also be used as a tool to further study the nanocomposite during mechanical and thermal processes.



PALS can provide insight to damage initiation in polymers and epoxies due to physical relaxation, cyclic strain or fast impact.

PAS may be used to evaluate fatigue in very early stages due to its sensitivity to nano-scale free volumes and may draw critical links between materials properties and chemical composition and/or cross-linking density. Works on polymeric fibers have shown direct correlation between the number of folding cycles and the varying degree of increase in the free volume voids detected by PALS. The damage only becomes obvious at much later stage using microscopy methods

Last but not the least, depth-profiled positron spectroscopies are useful in characterizing polymeric membranes for desalination or gas filtration where heterogeneous pore structure of multilayer films can be studied. The benefit of using positron as a probe in this type of studies is the fact that the activity and effect of the adsorbent can be monitored *in-situ*. PALS study on metal-organic framework (MOF) has directly revealed the evolution of nanostructure in MOF-5 during a monolayer adsorption of CO<sub>2</sub> molecules.



### Positron Intense Beam Facility and Defects Analysis Laboratory Characteristics



**Fig. 3.3.5 - A 3-D model and a picture of the constructed new generation Platinum based positron source**

The IPS produces positrons through pair production in a tungsten converter irradiated by high energy gammas from the reactor core, and from neutron capture in a cadmium end-cap surrounding the source (see Figure 3.3.5). Positrons emitted from the tungsten with kinetic energies of a few eV are accelerated to around 1 keV and focused electrostatically into a solenoidal magnetic field for transport out of the bio-shield. The IPS delivers a 25mm diameter beam with an intensity of  $6 \times 10^8$  positrons/second. With the high irradiation from the reactor core, significant defects are over time introduced into the tungsten moderators. These defects trap positrons and cause a drop in the positron rate. The surface of the tungsten also oxidizes that cause further rate drop. To replace the current tungsten positron converter, recently, a platinum based IPS has been constructed and is currently

being tested. This new generation IPS is expected to provide higher positron rate (on the level of  $1\text{-}3 \times 10^9$  positrons/second) and enhanced long term stability.

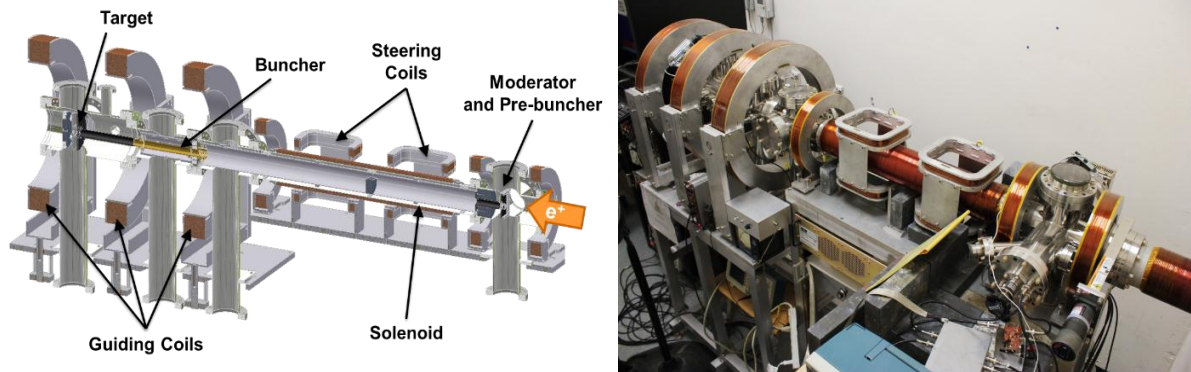


Fig. 3.3.6 - A schematic and a picture of the e<sup>+</sup>-PAS spectrometer

The main beam, once extracted from the main moderator, has a diameter of ~1 inch, and is transported through two magnetic switches and into adjacent labs that house two positron annihilation spectrometers. The first instrument, a Positron Annihilation Spectrometer (e<sup>+</sup>-PAS), uses a time varying electric fields to bunch positrons into sub-nanosecond pulses (*rep rate of 50 MHz, time resolution of 100 ps*) for positron lifetime studies in materials such as semiconductors and metals. The schematic and picture of the e<sup>+</sup>-spectrometer are shown in Figure 3.3.6 above.

The second instrument, a Positronium – Positron Annihilation Spectrometer (Ps-PAS), uses secondary electrons from the target for timing (*1 ns time resolution*) and is used to measure positronium lifetimes and to study free volumes and morphology in nano-porous materials, such as (but not limited to) polymer thin films, membranes, coatings, organic semiconductors, and low-*k* thin films. The Ps-PAS spectrometer is electrostatically focused with two-stage transmission brightness enhancement using 150 nm thick Nickel foils (see Figure 3.3.7).

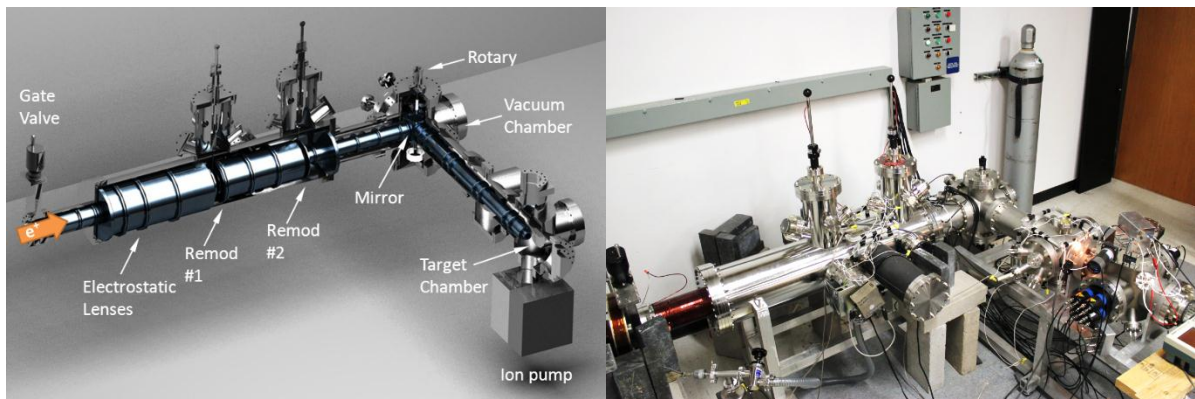


Fig. 3.3.7 - A schematic and a picture of the Ps-PAS spectrometer

The important parameters of the two spectrometers are shown in Table 3.3.1. The count rate on target in the e<sup>+</sup>-PALS spectrometer is approximately 6×10<sup>5</sup> e<sup>+</sup>/s due to the overall efficiency of positron remoderation, aperture cutting, and pre-buncher chopping. The optimum PALS timing resolution that has been achieved is 277 ps. Depending on the timing resolution requirement as realized by the settings of the chopping signal, it takes approximately 2 to 20 minutes to collect a PALS spectrum that contains 1 million total counts. In addition, by tuning the final drift lens potential according to sample bias as well as adding a collimated shield to the photomultiplier, systematic effects due to backscattered positron and positronium particles have been mostly eliminated. This would allow much better comparison among different beam energies without spectrum distortion under situations where heterogeneity of free volume distribution plays an important role.

**Table 3.3.1 - Important PALS parameters of the e<sup>+</sup>-PAS and Ps-PAS spectrometers based on positron rate of 5×10<sup>8</sup> e<sup>+</sup>/s from the IPS**

Spectrometer	On Target			Testing Beam
	e <sup>+</sup> /s	Spot Size	Spectrum FWHM	Energy
e <sup>+</sup> -PALS	6×10 <sup>5</sup>	10 mm	277 ps	15 keV
Ps-PALS	5×10 <sup>6†</sup>	2 mm	1 ns	5 keV

†estimated from single remoderator tests

In addition to the positron beam described above, a Na-22 based bulk PAS system is also currently operational at the PULSTAR reactor. This system can be used for the studying vacancy, vacancy cluster, or void concentration and size, etc. in various types of materials of millimeter level thickness. A diagram of the bulk system is shown in Figure 3.3.8. This system has complete digital signal processing and data acquisition enabled by a LeCroy Wavepro 7300A digital oscilloscope. The pulses from the PMTs are digitized and fitted with customized algorithm in real time to extract timing information, which results in a sub-200 ps timing resolution. Meanwhile, an analog system runs in parallel with the digital system for higher count rate experiments with lesser requirements on timing resolution.

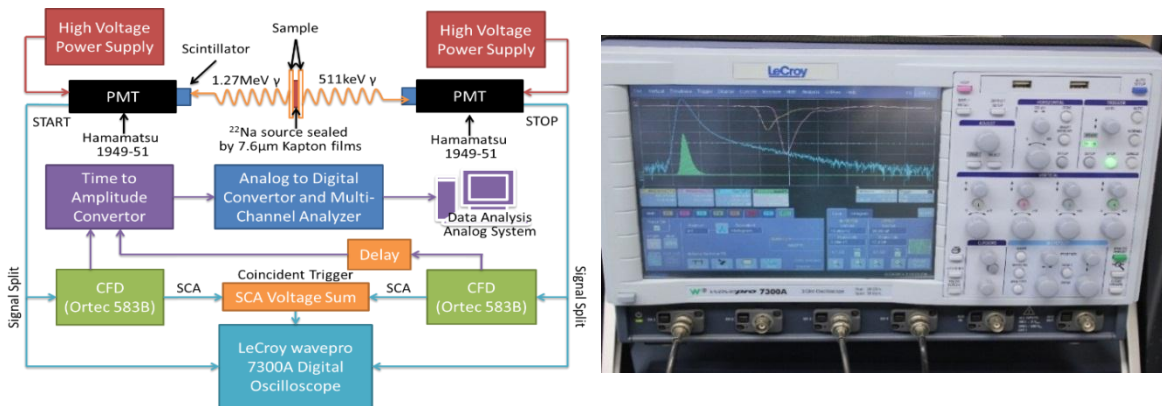


**Fig. 3.3.8 - Diagram of the bulk-PAS system and a picture of the digital oscilloscope showing a PALS spectrum.**

### 3.4 Ultra Cold Neutron Source

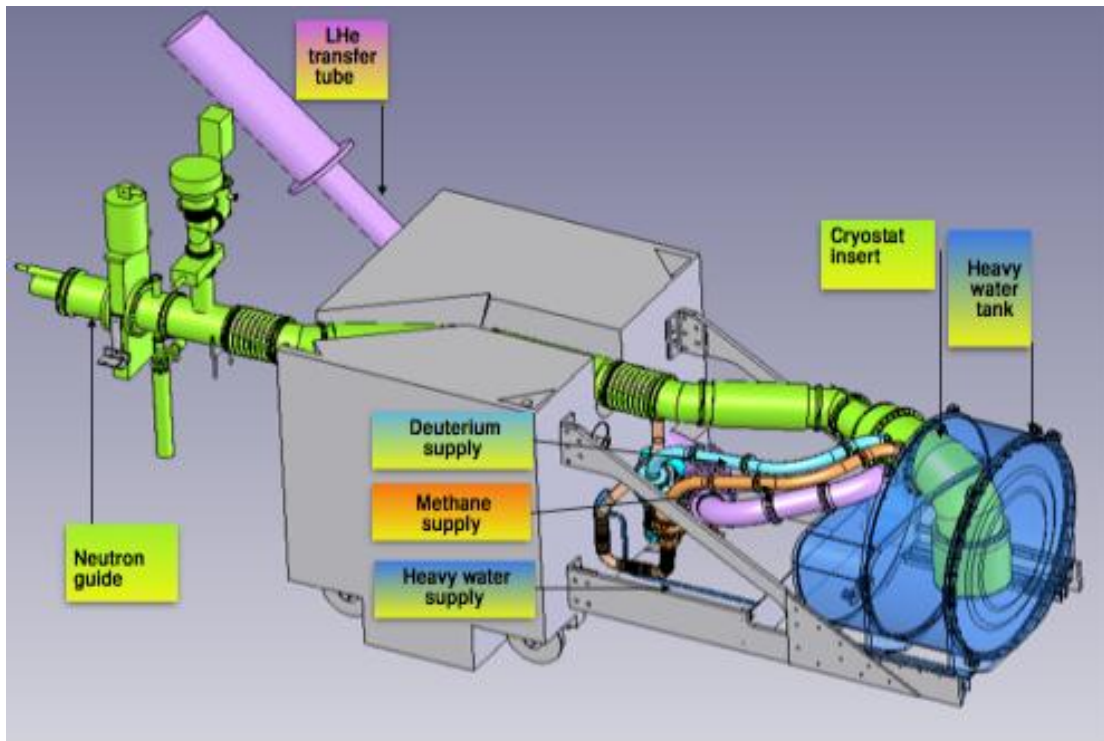


Fig. 3.4.1 – Ultra Cold Neutron Source

The PULSTAR Ultra-cold Neutron Source (UCNS) (see Figure 3.4.1) is designed to produce neutrons with energies below about 300 nano-electron Volts, or below temperatures of about 3 mK. These neutrons behave similar to light, in that they can reflect off of some material surfaces for any angle of incidence and therefore can be guided and stored in material bottles. Although ultra-cold neutrons are used primarily for fundamental physics studies of the properties of the neutron, they also have some application for non-destructive surface studies, an active area of research for the faculty at NCSU.

#### Applications of UCN's:

The capability of storing UCN is highly desirable for experiments, where ***fundamental properties of the neutron*** are studied, for instance, neutron Electric Dipole Moment (EDM) or neutron life time (See Figure 3.4.2). In these experiments the longer observation time and low velocities of neutrons leads to significant increase of experiment sensitivity. UCN storage is limited by the neutron beta-decay with  $\tau = 885$  sec.

In ***condensed matter applications*** it is the UCN selective probability of interaction that leads to the possibility of unique techniques to study surface and bulk properties of materials:

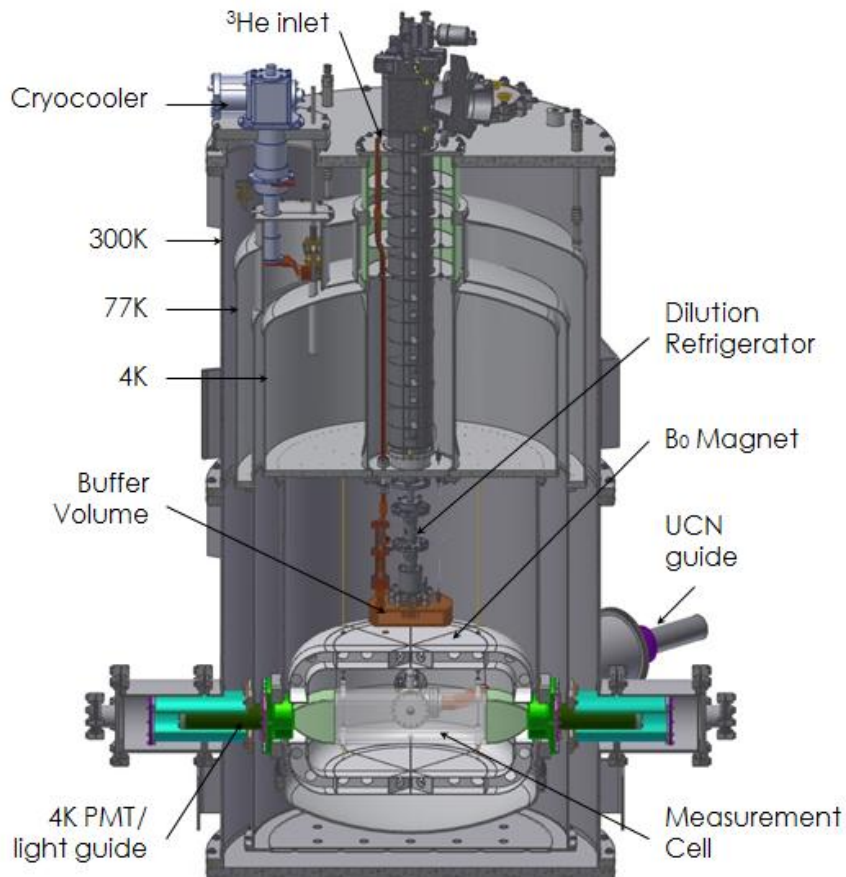


**Fig. 3.4.2 - Cryostat of the Neutron EDM Systematic study experiment** - An experiment to study magnetic interaction of polarized UCN and polarized He-3 as part of SNS, Oak Ridge, based neutron Electric Dipole Moment (EDM) project.

**Surface properties** (see Figure 3.4.3):

- Study of the inelastic incoherent scattering from nano-layers containing Hydrogen using storage of the low energy UCN, up to about 130 neV. Here the substrate, for instance, copper, is almost invisible, because UCN can penetrate into the bulk with probability  $10^{-4}$  per collision, whereas a Hydrogen film is a strongly interacting media.
- Surface profiling using prompt  $(n, \gamma)$  technique.
- Study of surface porosity, pinholes.

**Bulk properties:**

- UCN as a low energy neutrons are promising for developing a neutron scattering technique to study large, slow moving biological molecules.
- Study of scattering and absorption cross sections in homogeneous substances.
- Study of in-homogeneities in non-homogeneous substances.

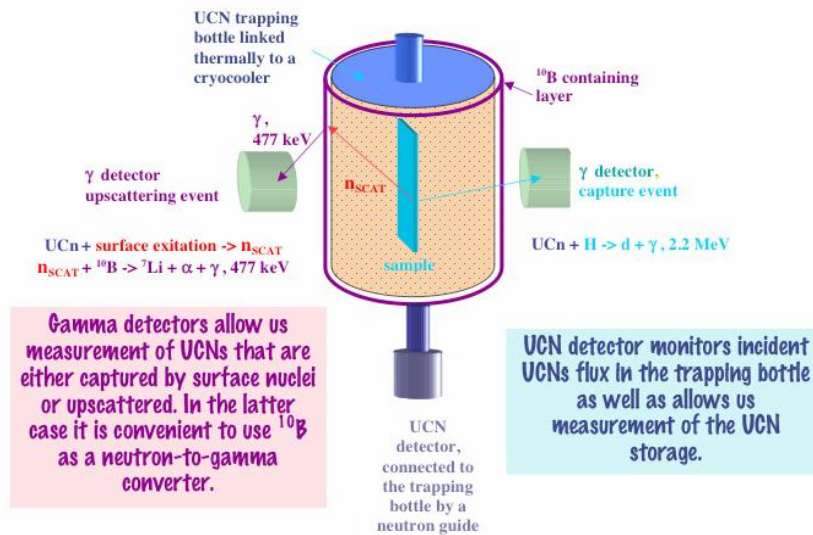


Fig. 3.4.3 – UCN Low Temperature Surface Study Experiment

### Characteristics of the UCN Facility

A graphite-lined nose port is used to couple the reactor face to the moderator geometry in the thermal column, where the source will be located. This geometry ensures minimal heating for the cryogenic source materials due to gamma-rays and fast neutrons from the reactor core. The source itself will be composed of one liter of solid deuterium, held at 5K and coupled to an ultra-cold neutron guide, held at 50K, inside of a nested set of thermal and cold moderators (See Figure 3.4.4). Ultra-cold neutrons are produced in the deuterium and then guided to experiments by extension of the room temperature guides.

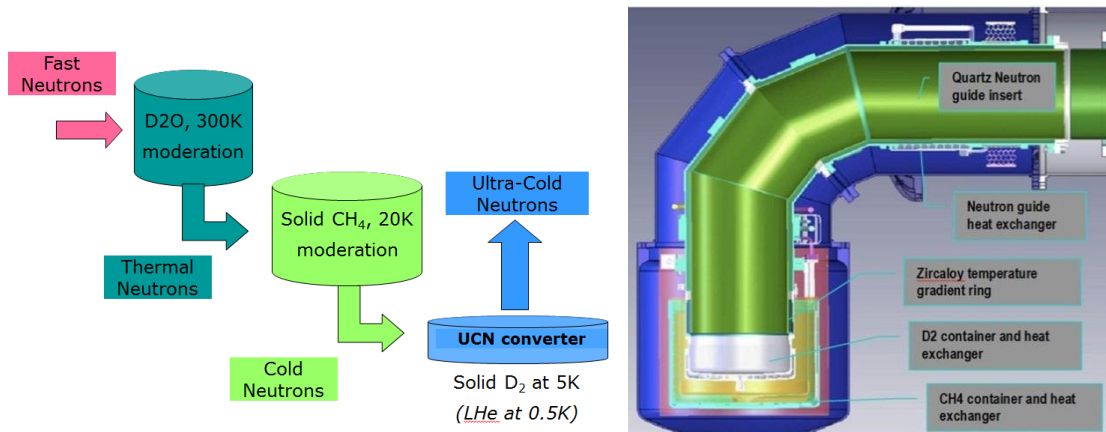


Fig. 3.4.4 – UCN source Moderator Assembly

Expected production rate of ultra-cold neutrons, based on MCNP simulations, is about  **$1 \times 10^4$  per cc per second**, resulting in world class UCN densities comparable to other leading UCN facilities in the world, such as the Institut Laue Langevin in Grenoble, France and LANL UCN source at Los Alamos, USA.

## 3.5 Internet Reactor Laboratory

Internet Reactor Laboratories (IRL) are available to external academic institutions who wish to utilize the PULSTAR in demonstrating nuclear reactor operations and kinetics for their students. This capability enriches academic programs at universities without research reactors of their own, and may be used to expand the educational opportunities for nuclear engineering students throughout the United States and internationally. IRL sessions are hosted from the PULSTAR reactor control room (see Figure 3.5.1) utilizing video conferencing and online reactor instrumentation and data acquisition systems.



**Fig. 3.5.1 – PULSTAR Control Room**

IRL participants are able to interact with reactor facility personnel through direct video and audio communication links, and have the ability to direct remote control cameras in the control room. An online data acquisition system is utilized to provide real time visualization of the reactor operating parameters (see Figure 3.5.2), and for collecting experimental data.

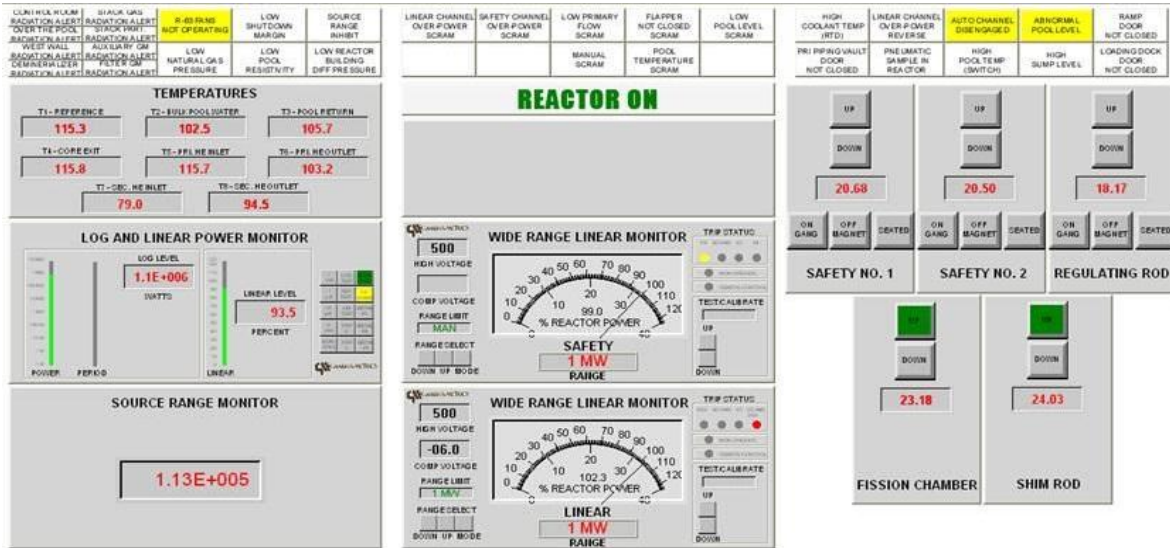


Fig. 3.5.2 – Internet Reactor Lab RTP-NetSuite Graphical User Interface

Examples of Internet Reactor Laboratory sessions that are available include:

- ❑ **Introduction to Reactor Plant Systems** - Review functionality and schematics of reactor instrumentation and SCRAM logic systems, primary and secondary cooling loops, and radiation monitoring and confinement systems.
- ❑ **1/M Approach to Criticality** - Use source range monitor count rate indication to plot projections for critical reactor control rod positions. Apply 1/M plot methodology to approach criticality conservatively.
- ❑ **Control Rod Calibration** (See Figure 3.5.3) - Measure the reactivity worth of a reactor control rod as a function of position. Withdraw the rod to place the reactor on a period and use the Inhour equation to determine the resulting reactivity addition. Plot differential and integral rod worth curves.
- ❑ **Power Defect Measurement** - Bring the reactor critical at incremental power levels between 100W and 1 MW. Measure the control rod reactivity worth at each power level and calculate power defect as a function of reactor power.
- ❑ **Axial Flux Mapping of a Fuel Assembly** - Utilize an in-core fission chamber to measure the flux distribution inside a fuel assembly. Plot flux distribution as a function of core height and determine the assembly average axial peaking factor.
- ❑ **Heat Balance Power Calibration** - Operate the reactor at several power levels up to 1 MW. Allow the reactor cooling system to stabilize at each level and record cooling loop temperature values. Use  $\Delta T$  values across the core and heat exchanger to perform a heat balance and determine true reactor power.

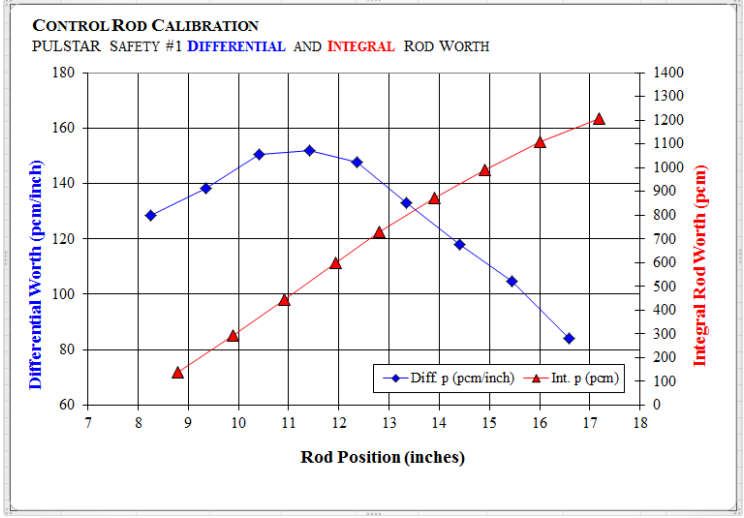


Fig. 3.5.3 – Control Rod Calibration Laboratory Session with Rod Worth Plot

### 3.6 Neutron Activation Analysis:



**Fig. 3.6.1 – Automated NAA Sample Analyzer**

Instrumental Neutron Activation Analysis (INAA) is one of the most sensitive analytical techniques used for the quantitative multi-element analysis of major, minor, and trace elements in samples from almost every conceivable field of scientific or technical interest. The technique of INAA measures the total amount of an element present in sample matrices without regard to chemical or physical form and without any pre-treatment of the sample. For certain elements, INAA offers sensitivities that are superior to those possible by other techniques; on the order of parts per billion or better. In addition to the elemental and isotopic analysis of samples, INAA permits the analysis of non-radioactive tracers introduced into biological, chemical, and/or industrial processes for process identification and optimization.

The NAA Laboratory (see Figure 3.6.1) utilizes the PULSTAR Reactor as an intense neutron source for the irradiation of client samples. During neutron irradiation, certain stable isotopes of elements that constitute the samples are transformed into radioactive isotopes by neutron capture. Activated trace radioisotopes (e.g. As-76, Hg-197, Se-75, etc...) contained in the samples are analyzed and quantified by utilizing gamma spectrometry systems to measure gamma ray decay signatures. Certified elemental standards, traceable standard reference material (SRM) controls, method blanks, and sample duplicates are processed along with client samples to maintain a high degree of quality assurance.

#### Advantages of using INAA for trace element analysis:

- It is a multi-element technique capable of determining approximately 65 elements (see Table 3.6.1 below) in many types of materials;

# NORTH CAROLINA STATE UNIVERSITY

**Table 3.6.1 – Elements Analyzed by NAA**

Ag, Al, As, Au, Ba, Br, Ca, Cd, Ce, Cl, Co, Cr, Cs, Cu, Dy, Er, Eu, F, Fe, Ga, Gd, Ge, Hf, Hg, Ho, I, In, Ir, K, La, Lu, Mg, Mn, Mo, Na, Nb, Nd, Ni, Os, Pd, Pr, Pt, Rb, Re, Rh, Ru, Sb, Sc, Se, Si, Sm, Sn, Sr, Ta, Tb, Te, Th, Ti, Tm, U, V, W, Y, Yb, Zn, & Zr.

- ❑ It is non-destructive and therefore, does not suffer from the errors associated with yield determinations;
- ❑ It has very high sensitivities for most of the elements that can be determined by INAA - most detection limits range from ~0.05 to ~50 ppm ( $\leq 1$  ppb for some high-purity materials)
- ❑ It permits the analysis of samples ranging in volume from 0.1 ml to 20 ml, and in mass from ~0.001 gram to 10 grams depending on sample density.
- ❑ Samples for INAA can be solids, liquids, gases, mixtures, and suspensions.



**Fig. 3.6.2 - High Purity Fused Silica & Industrial Sample Matrices**

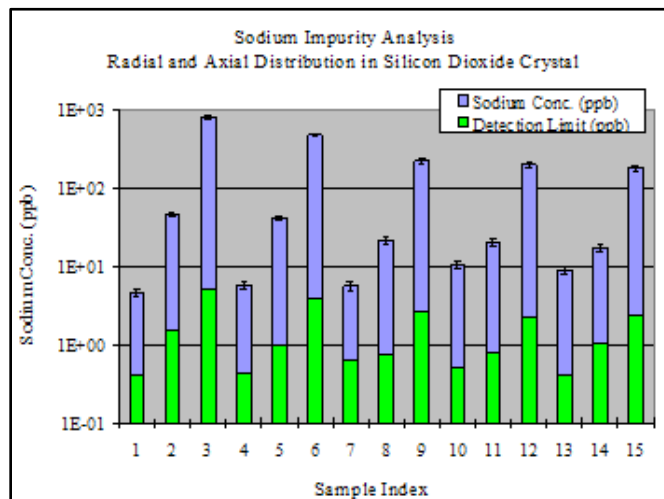


**Fig. 3.6.3 – Trace Sodium Analysis (ppb) in High Purity SiO<sub>2</sub>**

Examples of sample matrices previously analyzed at NCSU include:

- High purity silicon matrices (see Figure 3.6.2 – 3.6.3)
- Biological organs and tissues from laboratory research animals and fish
- Coal, crude oil, diesel fuel
- Fertilizer
- Forensic investigation samples (e.g. fibers, tissue, hair, bullets)
- Graphite
- Geologic specimens
- Human nails, urine and hair
- Industrial process samples (e.g. hydrocarbons, resins) (see Figure 3.6.2)
- River and tailing pond sediment
- Textile fibers

### 3.7 Reactor Irradiations and Isotope Production

The irradiation of materials, samples, and nuclear instrumentation may be carried out in any one of the numerous penetrations adjacent to the PULSTAR reactor core. Existing penetrations range in inner diameter (ID) from 1.25 inches to 8 inches (with one radial port 12 inches square) and have varying neutron and gamma energy spectra and intensities (see listed in Table 2.1, and pictured in Figure 3.7.1 below).

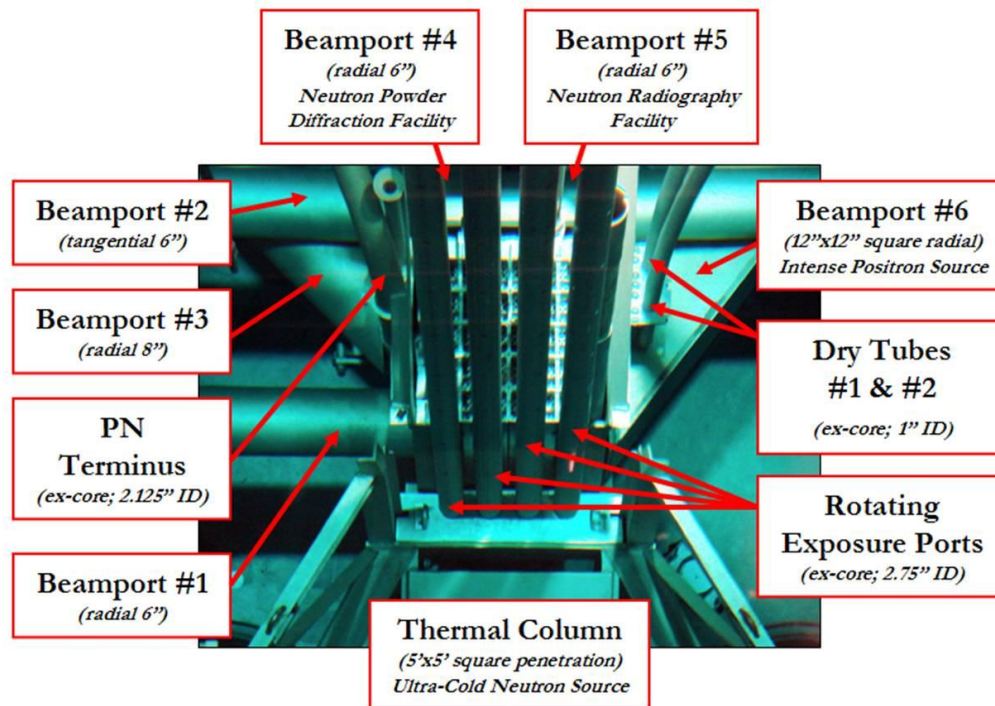


**Fig. 3.7.1 – Reactor Irradiation Penetrations**

In addition to those irradiation facilities already available, custom experimental facilities can be developed to accommodate different experiment geometries and spectral requirements.

Examples of irradiation projects include:

- Irradiation of materials in high temperature environments (See Figure 3.7.2).
- Accelerated lifetime testing of ex-core neutron compensated ion chambers, fission chambers, and BF<sub>3</sub> detectors (See Figure 3.7.3).
- Sensitivity evaluation of in-core (miniature) neutron fission chambers.
- Measuring radiation damage in fiber optic stress sensors.
- Radiation hardness testing of electronic nuclear instrumentation modules.
- Transmutation doping of Silicon wafers.

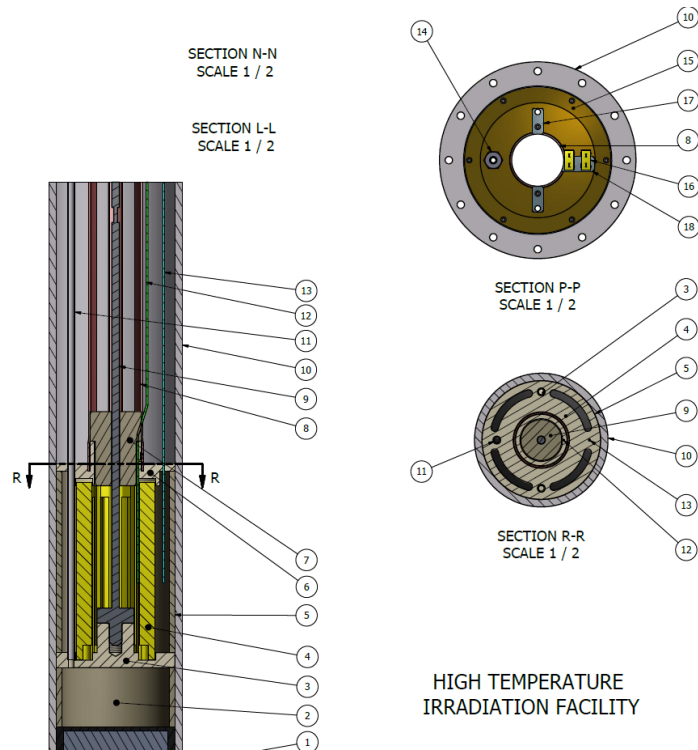


**Fig. 3.7.2 – High Temperature Irradiation Facility Schematic; sample chamber 1.5” ID x 4” high; currently 600°C max, heater upgrades planned.**

**Isotope Production:**

Radioisotopes have various research and industrial applications, including in medicine, life sciences, and industrial processes. As an alternative to the direct use of radioactive materials in some applications, stable tracers that incorporate elements such as gold, samarium, indium, and gadolinium can be formulated, introduced into processes, and concentrations subsequently determined via neutron activation analysis.

The PULSTAR reactor is available to produce millicurie quantities of many radioisotopes for approved, licensed use. Examples of isotopes that have been produced at NCSU for R&D purposes include: Au-198, Br-82, Co-60, Ho-166, K-42, Mn-56, Na-24, and Sb-124.

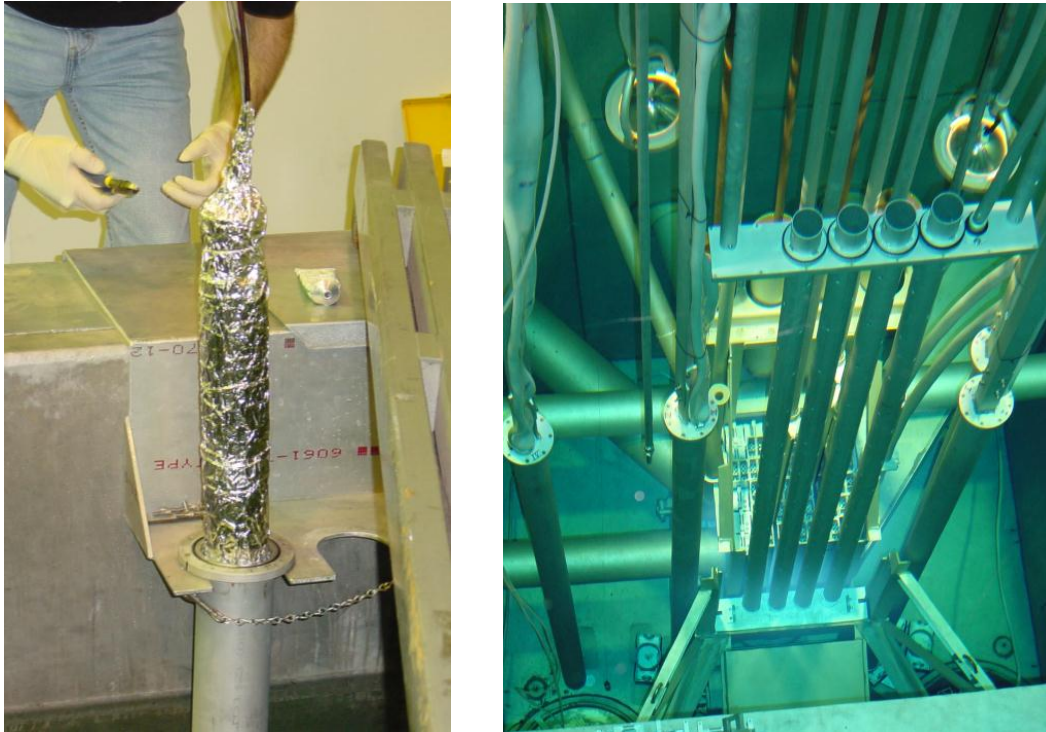


**Fig. 3.7.3 – Irradiation Testing of Ex-Core Neutron Detectors to  $1E18$  NVT Thermal Fluence in 3500 MW-hrs exposure. 3.5" ID Standpipes utilized (at right).**

## Appendix A: Analysis of Nuclear Graphite using the Neutron Powder Diffraction Facility and Microstructure Analysis Laboratory

### Introduction

Graphite is an important nuclear material that can be used as moderator and major structure components in modern nuclear reactor designs such as the Very High Temperature Reactor (VHTR) and the Advanced High Temperature Reactor (AHTR) because of its low thermal neutron absorption cross section, small atom number, and stability at high temperature. Nuclear graphite is polycrystalline and is characterized by its high degree of graphitization, random bulk orientation and high chemical purity. This material is multiphase and contains a coal-tar binder phase and a petroleum-coke filler phase. Upon heating to nearly 3000 °C the petroleum-coke phase achieves a high level of crystallinity[1].

The triperiodic structure of graphite can be considered as sheets of C atoms arranged in a honeycomb pattern stacked in an ABAB or ABCABC sequence. Strong covalent bonds exist within plane, and weak Van der Waals bonds exist between the neighboring layers. The interlayer distance is 3.35Å, which is much larger than the distance between the nearest neighbors in the layer (1.42Å). The density of reactor grade graphite is in the range of 1.5 to 1.8 g/cm<sup>3</sup>, which is much less than that of single crystal graphite due to being a highly porous material [1].

Nuclear grade graphite is considerably less perfect than single crystals graphite, and the fast neutron irradiation damage can increase this kind of imperfection. Neutron powder diffraction is a powerful method to investigate the imperfection of graphite. Bragg's peak positions are related to the average d-spacing, and the width of the peaks can give the information of stacking fault, crystallite size, and the fluctuation of the d-spacing. At the least perfect end, only the (00l) and (hk) reflections can be found in the diffraction pattern. The (00l) peaks is resulted from parallel stacking of layer plane, and the two-dimensional (hk) peaks is resulted from the hexagonal structure in the individual layer plane. It is of great interesting to study the change of the crystal structure of reactor grade graphite after fast neutron irradiation.

In this paper, we present the neutron diffraction patterns of two nuclear grade graphite specimens. One is un-irradiated; the other one is irradiated at 280 °C. The first one has graphite structure and is analyzed by the two-layer structure model introduced by reference [2] [3]. The second one is totally turbostratic disordered and is analyzed by the one-layer model introduced by reference [2]. The refinement results indicate that the irradiation damage can increase the probability of stacking fault, d-spacing, the fluctuation of d-spacing, and decrease the probabilities of AB and ABC stacking, the stacking number of the layers, the lattice parameter in the plane, and the lateral dimension of the plane.

**Radiation Damage in Reactor Grade Graphite**

Radiation damage in graphite arises overwhelmingly from fast neutrons. Fast neutron radiation damage happens when the carbon atoms are displaced from their lattice positions, and produce the vacancy/interstitial pairs. Graphite interstitials preferentially congregate in the interlayer gap due to relatively large interlayer space. These interstitials, as well as the vacancies, can coalesce into more complex structures such as the interstitial and vacancy loops shown schematically in Figure 1. As the dose increase, the interstitial loop can grow up and form a new graphite layer, and the vacancy loop, on the other hand, may cause the inward collapse of nearby layers.

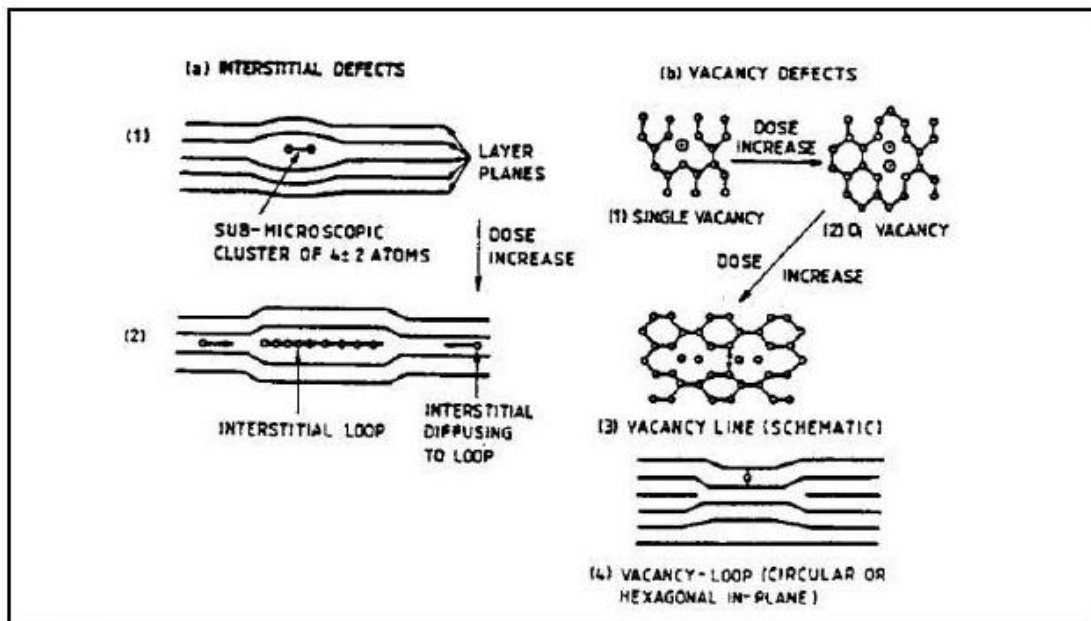
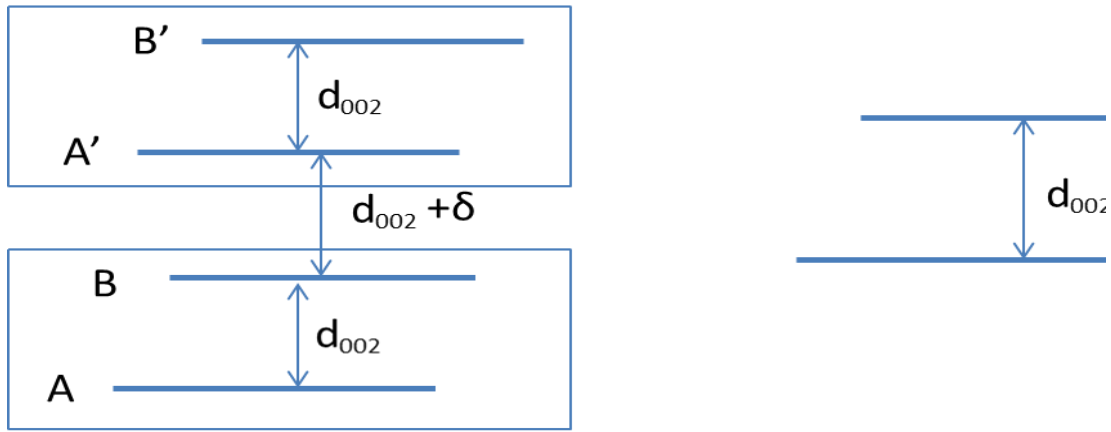


**Fig. 1: the model of defect aggregations in graphite [4].**

**Models of Reactor Grade Graphite Structure**

The models of graphite structure we adapted are the models introduced by [2][3]. There are two models, one is two-layer model and the other one is one-layer model. The basic unit of the two-layer model is a two AB registered stacking layers package with finite lateral extent. The d-spacing between the two layers is  $d_{002}$  without fluctuation. The three stacking options are as following: (see Figure 2(a))

- 1) A random shift between the adjacent packages with probability  $P_r$ . The two packages have no phase correlation.
- 2) A registered shift between the adjacent packages with probability  $P_t$ . The A layer in the package above move to the C stacking reference to the A layer in the package below, and the B layer in the package above will move to the A stacking reference to the A layer in the package below. Local ABC stacking appears.
- 3) No shift at all with probability  $(1-P-P_t)$ , which give local ABAB stacking.



a) Two-layer model

b) One-layer model

Fig. 2: The two models introduced by [2] [3]. The bold line represents the basal layer.

Clearly, this model can model the ABAB... stacking ( $P=P_t=0$ ), the ABCABC... stacking ( $P=0$ , and  $P_t=1$ ), and the graphite with some ABC and/or random shift stacking faults. But it can not model the structure with the probability of stacking fault above 0.5, since half the neighboring layers are constrained with AB stacking.

A parameter  $\delta$ , where  $\langle\delta\rangle=0$ , and  $\langle\delta^2\rangle\neq 0$ , was introduced to model the d-spacing fluctuation. It is assumed that the d-spacing fluctuation is only happened between the two packages. The probability of a given fluctuation  $\delta$  follows the Gaussian distribution:

$$p(\delta) = \frac{1}{\sqrt{2\pi\langle\delta^2\rangle}} e^{-\delta^2/(2\langle\delta^2\rangle)} \quad (1)$$

In the one-layer model shown in Figure 2b, the basic unit is a carbon layer with graphite honeycomb arrangement, which is then stacked to form the carbon. If a particular layer is said to occupy the A position, then the next layer can be:

- 1) A random shift layer with probability P;
- 2) A layer occupied the B position with probability  $(1-P)/2$ ;
- 3) A layer occupied the C position with probability  $(1-P)/2$ .

This model can not reproduce the ABAB... and ABCABC... stacking found in crystalline graphite, but it can describe the most disordered carbon adequately. For the totally turbostratic disordered carbon, the probability of random shift layer should be 1.0.

A combination of a Dirac delta function and a Gaussian distribution is given to describe the d-spacing fluctuation. The formula is given as following:

$$P(\delta) = g\delta_D(\delta) + (1 - g) \frac{1}{\sqrt{2\pi \langle \delta^2 \rangle}} e^{-\delta^2 / (2\langle \delta^2 \rangle)} \quad (2)$$

In the first term in equation (2),  $g$  is a number between zero and one, which represents the fraction of low-strain portion in graphite. In the second term, the Gaussian distribution represents the portion in graphite with d-spacing fluctuation.

There are other parameters of these two models, such as the in-plane lattice constant, number of the basic unit in the two models, lateral size of the crystallite, the preferential orientation, the isotropic temperature factor, and the in-plane strain parameter. All these parameters are listed in Table 1.

**Table 1: Parameters used in the two-layer package model and one-layer model introduced by [2] [3].**

Parameters	Two-layer model	One-layer model
Inter planar spacing	$d_{002}$	$d_{002}$
In-plane lattice constant	$a$	$a$
Probability of random shift between adjacent unit	$P$	$P$
Probability of 3R stacking between two adjacent unit	$P_t$	
Fraction of unorganized carbon		$(1-g)$
In-plane strain parameter		$\zeta$
Fluctuation of d spacing between adjacent two layers	$\frac{1}{2} \sqrt{\langle \delta^2 \rangle}$	$\sqrt{\langle \delta \rangle^2}$
Number of stacking units in the crystallite	$M$	$M$
Lateral size of the crystallite	$L_a$	$L_a$
Preferred orientation	$P_0$	$P_0$
Isotropic temperature factor	$B$	$B$

### Analysis of Neutron Powder Diffraction Pattern According to Above Models

Based on the above models, the idea for calculating the diffraction intensity of graphite is considering a whole layer as a giant crystal diffracting unit, repeated more or less regularly along a single direction.

For a single layer with finite extent, it can be characterized by a function as following [5]:

$$C(\vec{r}) = b(x, y, z) \otimes [\{\sum_{P_1} \sum_{P_2} \delta(\vec{r} - P_1 \vec{a}_1 - P_2 \vec{a}_2)\} \cdot g(x, y, 0)] \quad (3)$$

Where  $b(x, y, z)$  is neutron scattering length in the unit cell;  $g(x, y, 0)$  is the shape function;  $\vec{a}_1, \vec{a}_2$  are base vectors of the plane lattice;  $P_1, P_2$  are two integers; and  $\vec{r}$  is vector characterizing the position of a point in plane.  $\otimes$  is the convolution operator.

The amplitude of the neutron diffracted by one individual layer is given by the Fourier transform of  $C(\vec{r})$ :

## NORTH CAROLINA STATE UNIVERSITY

---

$$\Phi(\vec{s}) = \frac{F(\vec{s})}{\Omega} \cdot [\{\sum_h \sum_k \delta(\vec{s}_0 - h\vec{b}_1 - k\vec{b}_2)\} \otimes D(X, Y, \infty)] \quad (4)$$

Where  $F(\vec{s})$  is the structure factor,  $\vec{s}$  is the scattering vector,  $\Omega$  is the area of unit cell,  $h$  and  $k$  are Miller indices,  $\vec{b}_1$  and  $\vec{b}_2$  are the base vector of the reciprocal lattice, and  $D(X, Y, \infty)$  is the Fourier transform of the shape function.  $X$ , and  $Y$  are the components of  $\vec{s}$  in the basal plane.  $D(X, Y, \infty)$  decreases along  $X$  and  $Y$  fairly rapidly, and it can be approximated as:

$$D(X, Y, \infty) \approx D(\epsilon_1, \epsilon_2, \infty)$$

$$\text{Where } X = hb_1 + \epsilon_1 \text{ and } Y = kb_2 + \epsilon_2.$$

For a perfect isolated layer, the intensity of the diffraction beam is:

$$I(\vec{s}) = \Phi(\vec{s})\Phi^*(\vec{s}) = \frac{|F(\vec{s})|^2}{\Omega^2} [\{\sum_h \sum_k \delta(\vec{s}_0 - h\vec{b}_1 - k\vec{b}_2)\} \otimes \eta(\epsilon_1, \epsilon_2, \infty)] \quad (5)$$

$$\text{Where } \eta(\epsilon_1, \epsilon_2, \infty) = D(\epsilon_1, \epsilon_2, \infty)D^*(\epsilon_1, \epsilon_2, \infty)$$

According to formula (5), the diffraction beam intensity is localized along the “rod” ( $hk$ ) of infinite length, of basal area  $\eta(\epsilon_1, \epsilon_2)$ , centered on the  $hk$  nodes of the reciprocal lattice and perpendicular the plane of this lattice, as shown in Figure 3.

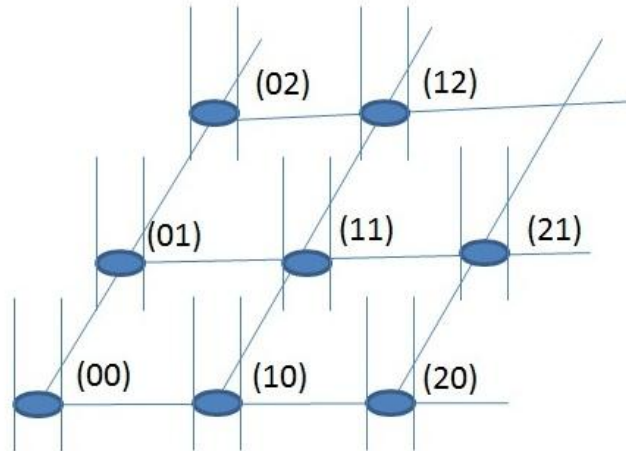


**Fig. 3: The reciprocal lattice of a single two dimensional graphite layer. The Miller indices are labeled beside each node.**

In formula (5),  $\eta(\epsilon_1, \epsilon_2, \infty)$  is independent of  $h$  and  $k$ , the radius of each rod is same at every  $hk$  node. In order to include the influence of layer strain on rod radius, a refinable parameter  $\zeta$  is introduced to simulate in-plane strain, and write  $\eta(\epsilon_1, \epsilon_2, \infty)$  as [6] [7]:

$$\eta(\epsilon_1, \epsilon_2, \infty) = \frac{L_a^2}{a^2} \frac{\omega}{\omega + \zeta s_0} e^{-|\vec{\epsilon}|^2 / (\omega + \zeta s_0)^2} \quad (6)$$

$$\text{Where } \omega = 2 / (L_a \sqrt{3\pi})$$

For a stack of graphite layers, the average diffraction intensity is given by [2] [5]:

$$i(\vec{s}) = M |\Phi(\vec{s})|^2 G(\vec{s}) \quad (7)$$

Where M is the number of layers (one-layer model) or two-layer packages (two-layer model),  $G(\vec{s})$  is the modulation function. If the stacking of each nearest neighbor pair is independent of neighboring layers,  $G(\vec{s})$  can be given as [2] [5]:

$$G(\vec{s}) = \text{Re} \left[ \frac{1+q}{1-q} + \frac{2}{M} \frac{q^{M+1}-q}{(1-q)^2} \right] \quad (8)$$

Where q is the average phase factor of the nearest neighbor pair, and is given by:

$q = \langle e^{2\pi i \vec{s} \cdot \Delta \vec{r}} \rangle$ , and  $\Delta \vec{r}$  is the translation between nearest neighbor, and q can be calculated according to the above two models.

Formula (7) gives the diffraction intensity of a small-size single crystal. Since reactor grade graphite is a polycrystalline material,  $i(\vec{s})$  should be powder averaged in order to make comparison with the observed data. The powder average can be obtained by keeping the reciprocal lattice fixed and considering the intersection of each (hk) rod with a sphere centered on origin of the reciprocal lattice with radius s. Therefore, for (hk) rod considered, the powder intensity is an angular average in reciprocal space [5]:

$$I_{hk}(s) = \int i_{hk}(\vec{s}) \frac{dA}{4\pi s^2} \quad (9)$$

In the case of the radius of rod is much smaller than the length of the size of reciprocal base vector, the tangent cylinder approximation [8] can be used, and the final diffraction intensity  $I_{hk}(s)$  is:

$$I_{hk}(2\theta) = I_{hk}(s) = \frac{M}{4\pi s} |F_{hk}(Z)|^2 \frac{L_a^4}{a^4} \frac{\omega^2}{\omega + \zeta s_0} \int_{-\pi/2}^{\pi/2} d\varphi G_{hk}(s, \psi) e^{-2(s \cos \varphi - s_0)^2 / (\omega + \zeta s_0)^2} e^{-PO \cos^2(\varphi)} \quad (10)$$

Where  $s = 2 \sin \theta / \lambda$ , and PO is the preferred orientation parameter.

The final diffraction intensity at  $2\theta$  is:

$$y_{ci} = \text{scale} \left[ (I_{00}(2\theta) + 6I_{10}(2\theta) + 6I_{11}(2\theta) + 6I_{20}(2\theta) + 12I_{21}(2\theta)) \otimes g(2\theta) \right] + b$$

Where scale is refineable parameter in order to march the observed data, the factor 6 and 12 are due to the 6-fold rotation axis at (00) node,  $g(2\theta)$  is a Gaussian function due to the resolution of instrument, and b is the background function. The other (hk) rods not included in last formula are outside the scale of our measurement.

# NORTH CAROLINA STATE UNIVERSITY

---

In order to compare the difference between the calculated and observed intensity, the residual  $S$  is defined as following:

$$S = \sum_i \omega_i (y_i - y_{ci})^2$$

Where  $i$  is the step number,  $y_i$  is the observed intensity at  $i$ th step,  $y_{ci}$  is the calculated intensity at the  $i$ th step, and  $\omega_i$  is the weight factor at  $i$ th step. It is  $1/y_i$ .

The goodness of fit ( $\chi^2$ ) is defined as:

$$\chi^2 = \frac{S}{N - P}$$

Where  $N$  is the total number of steps, and  $P$  is the number of refined parameters.

A Rietveld like non-linear least squares method is applied to minimize the residual between the observed and calculated intensity. The detail algorithm and programming techniques involved to implement the refinement are given in reference [9].

## Experimental

Neutron diffraction measurements were carried out at the PLUSTAR Neutron Powder Diffractometer at the NC State University. The PLUSTAR reactor is a swimming pool reactor with maximum power 1MW. The diffractometer is located at the beam tube 4 of the reactor. A double focusing monochromator, which can focus two-dimensional neutrons to the sample position, is employed in this facility. The flux of neutrons with wavelength 1.479 Å is  $0.5 \times 10^5$  n/cm<sup>2</sup>s at the sample position. A 15 position sensitive detector array is attached to a moveable cassette which allows the distance between sample and detector array be changeable in the range of 1.1m to 1.6m. The detector array spans 20° and can be moved from 15° to 115° to cover the entire scattering angle of 5°-125°. A fission chamber located at the beam before the sample is employed as the monitor. The detectors collect data at each section for a fixed monitor count to ensure the incoming neutron at sample position is same for each section. At last, the 6 sections data will be rebounded into a full scattering angle range data.

There are two nuclear grade graphite specimens. One is un-irradiated (NBG-10), and the other one (L25) was irradiated at 280 °C with total dose  $4.9 \times 10^{25}$  n/m<sup>2</sup>.

## Results and Discussion

The un-irradiated specimen maintains its graphite structure. Its neutron diffraction pattern is fitted by the two-layer model, and the irradiated specimen has totally turbostratic disorder since there are no three dimensional peaks. Its neutron diffraction pattern is fitted by the one-layer model. Their neutron diffraction patterns are shown in Figure 4a and 4b, and their refined parameters are given in Table 2. A calculated neutron diffraction pattern with the standard Rietveld refinement code (FULLPROF) is given in figure 4c, this pattern is quite different with the two observed ones, since the standard Rietveld

## NORTH CAROLINA STATE UNIVERSITY

refinement code cannot simulate the defects in reactor grade graphite. The parameters in Table 2 (below) can be classified as axial stacking parameters:  $d_{002}$ ,  $\langle\delta^2\rangle$ , M, P, and  $P_t$ ; the plane structure parameters: a, and  $L_a$ ; the atom thermal motion parameter B, and the preferred orientation parameter  $P_0$  of the specimen. According to Table 2, we can find that the irradiation damage reduces the probabilities of ordered AB and ABC stacking, the number of the layers stacked in one crystallite, the lattice parameter a, the lateral dimension; and increases the probability of randomly stacking, the isotropic temperature factor, the inter-layer d spacing and its fluctuation.

**Table 2: The results of the un-irradiated and irradiated graphite samples.**

Parameters	NBG-10 (un-irradiated)	L25 (irradiated at 280 °C)
$d_{002}$ (Å)	3.3677(1)	3.462(1)
a (Å)	2.4598	2.4069(9)
P	0.4412(16)	1.0*
$P_t$	0.1340(17)	
$1-P-P_t$	0.4248	0.0
$\langle\delta^2\rangle$ (Å <sup>2</sup> )	0.0109(1)	0.31(2)
G		0.40(2)
Z		0.0661(8)
M	70(2)	8.3(3)
$L_a$ (Å)	539(19)	42.45(8)
$P_0$	0.0*	0.0*
B (Å <sup>2</sup> )	0.700(6)	1.28(5)
$\chi^2$	3.5	1.8

\* fixed in refinement

The displaced carbon atoms favor going to the interlayer space due to the relatively large interlayer space. The interstitial atoms can move and form interstitial loops, and these loops will increase the interlayer d spacing locally, and increase the average interlayer d spacing and its fluctuation. At the same time, the existence of the interstitial atoms and loops will force their neighbor layers shift randomly, and the probability of random shifting increased.

The vacancy defects in the crystal lattice can distort the lattice in the plane locally, and this distortion will cause the contraction along the a axis and the entire lateral dimension. The vacancy defects in the crystal lattice may join together to form vacancy loop which may collapse the basal planes, and the total number of two-plane packages in the crystallite is reduced. The existence of vacancy defects affects the environment of their neighbor carbon atoms, and the isotropic temperature factor increases.

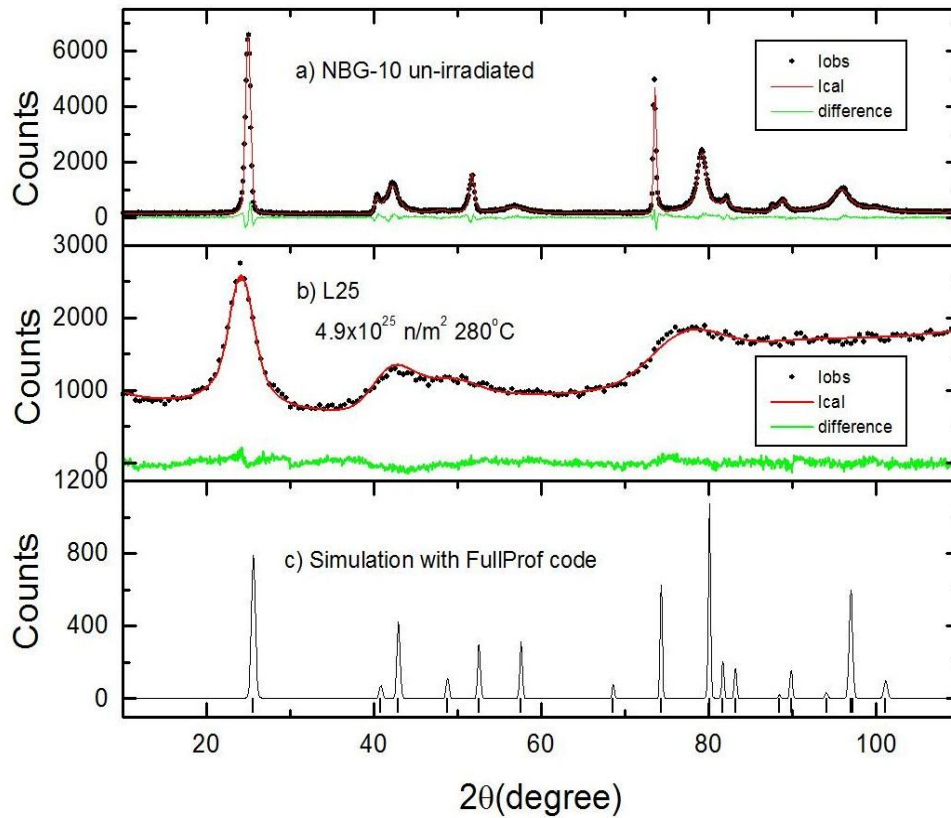


**Fig. 4:** The neutron diffraction patterns of reactor grade graphite specimens. The black points are the observed data, the red line is the calculated data, and the green line is the difference of observed and calculated data.

### Conclusions

The neutron powder diffraction technique is applied to study the irradiated and un-irradiated reactor grade graphite samples. Comparing to the x-ray diffraction pattern, the neutron diffraction pattern can give more information at the high angle range. The un-irradiated sample maintains its graphite structure with some stacking faults and d-spacing fluctuation, but the irradiated sample is totally turbostratic disordered. A Rietveld-like refinement code using Shi's models was implemented to interpret the powder diffraction patterns of the two specimens. Using these two models an assessment was made of the nature of disruption in the reactor grade graphite microstructure.

### Acknowledgments

The authors would like to thank Dr. T. Burchell of Oak Ridge National Laboratory for supplying the graphite samples. This work was partially supported by funding from the DOE NEUP program.

## References

- [1] Nightingale, R. E. Nuclear Graphite, Academic Press, New York, 1962.
- [2] H shi, J.N. Reimers, J.R. Dahn, J. Appl. Crystallogr. 26 (1993) 827.
- [3] D.D. DiJulio, A.I. Hawari, Journal of Nuclear Materials 392 (2009) 225.
- [4] B.J. Marsden, Siu-Lun Fok, Haiyan Li, 18<sup>th</sup> International Conference on Structural Mechanics in Reactor Technology (SMiRT 18) Beijing, China, Aug. 7-12, 2005.
- [5] Victor A. drite, Cyril Tchoubar, "X-ray Diffraction by Disordered Lamellar Structures" Springer-Verlag, 1991.
- [6] S. Ergun Carbon, 14, 139 (1976)
- [7] S. Ergun "Physics and Chemistry of Carbons", vol 3 edited by P. L. Walker Jr. 1968
- [8] G. W. Brindley, J. Mering Acta Crystallogr 4, 441, 1951
- [9] W.H. Press, S.A. Teukolsky, W.T. Vetlering and B.P. Flannery, "Numerical Recipes in Fortran: The art of scientific Computing" second edition, Cambridge University Press.

**Appendix B: Characterization of Defects in Nuclear Graphite Using the Positron Intense Beam Facility and Defect Analysis Laboratory**

**Radiation Damage to Nuclear Graphite**

The NC State Positron Intense Beam Facility and Defect Analysis Laboratory provides both bulk and beam positron annihilation spectroscopy (PALS and DBS) capabilities that have been used for a wide variety of materials characterization tasks. Recently, for example, neutron induced damage of a series of reactor-grade (i.e., nuclear) graphite samples (NBG-10) exposed to an intense flux of neutrons were studied with PALS, and in portfolio with other characterization techniques including scanning electron microscopy (SEM), mercury intrusion porosimetry (MIP), X-ray diffraction (XRD). Reactor-grade graphite is utilized as a neutron moderator/reflector and a structural component in various concepts of advanced thermal fission reactors including the very high temperature reactor (VHTR) and the advanced high temperature reactor (AHTR). Consequently, the graphite is exposed to an intense flux of neutrons that initiates the displacement of lattice atoms and the creation of vacancy and interstitial Frenkel pairs. The migration and agglomeration of these point defects leads to effects that can alter both the structural and neutronic behavior of the reactor-grade graphite. In this work, neutron induced damage in graphite is studied at the atomic scale using PALS. More specifically, the positrons, after being implanted into materials, can naturally diffuse to and be trapped in free volumes, and subsequently decay with characteristic lifetimes, which can be associated with the properties of vacancy-type defects.



**Fig. 1 – Nuclear Graphite Study Samples**

Three Samples of NBG-10 reactor-grade graphite were utilized in this study. The first sample was not irradiated. The other two samples of NBG-10 (see Fig. 1) were irradiated by fast neutrons (>1 MeV) at the HFIR reactor of Oak Ridge National Laboratory, with fast fluences of  $4.9 \times 10^{25} \text{ n/m}^2$  at 280°C (L25), and  $4.7 \times 10^{25} \text{ n/m}^2$  at 700°C (L69), respectively. These samples

were characterized in comparison with the un-irradiated pristine NBG-10 sample as well as a paralytic graphite and single crystalline copper as standards.

In contrast to the well-ordered stacking structure of ideal graphite, reactor-grade graphite has randomly oriented graphitic domains exhibiting cracks as well as non-graphitic regions with containing pores. This two-phase semi-crystalline structure, which results from the graphitization process of the filler particles and their imbedding matrix (the binder), was observed in a number of studies. The electron microscopy image also suggested a complicated microstructure with a hierarchy of free volume scales that should be associated with structural defects as well as non-graphitic regions, which is also confirmed by MIP measurement. However, no obvious structural difference was seen by SEM among the virgin and irradiated samples.

For the two irradiated samples, L69 and L25, the PALS spectra were distorted by their own radioactivity due to neutron activation. These gamma-rays and their subsequent Compton scattering events produce false coincident counts in addition to the real positron annihilations. In order to correct for this effect, the spectra of the two irradiated samples were taken with and without the  $^{22}\text{Na}$  source under identical conditions so that the corrected spectra can be obtained by subtracting the no-source spectra from the with-source spectra. After the correction, the spectra were fitted using the POSFIT routine, with two or three discrete lifetime components. According to calibration measurements of single crystalline copper with widely known positron lifetime of 110 ps, the Kapton seal and the source itself introduced a positron lifetime of 380 ps with 11% intensity, which was corrected for all the three samples. In addition, a pair of single crystalline copper pieces was also measured in order to calibrate the shape of the prompt peak.

**Table 1 – PALS Results for Nuclear Graphite**

Sample	$\tau_1$ (ps)	$I_1$ (%)	$\tau_2$ (ps)	$I_2$ (%)	$\tau_3$ (ns)	$I_3$ (%)
NBG-10 (0 n/m <sup>2</sup> )	208±5	28.5±0.5	422±2	70±1	2.1 (fix)	0.71±0.03
L25 (4.9×10 <sup>25</sup> n/m <sup>2</sup> at 280°C)	---	---	368±5	98.3±0.2	2.1 (fix)	1.7±0.1
L69 (4.7×10 <sup>25</sup> n/m <sup>2</sup> at 700°C)	235±10	31±3	397±5	69±3	2.1 (fix)	0.1±0.1

The POSFIT analysis results are summarized in Table 1. In a perfect graphitic structure, the positron lifetime was predicted and found to be 204 and 208 ps [12, 13]. In this study, the PALS spectra of the unirradiated NBG-10 were well fitted with three lifetime components. The first two short lifetimes (See  $\tau_1$  and  $\tau_2$  in Table A1) of ~200 ps and ~400 ps are attributed to positrons annihilating in the point defects of the graphitic phase and the nanovoids or boundaries in the vicinity of disordered structures, respectively. More accurately, according to the trapping model, the  $\tau_1$  of NBG-10 should be an average of both positrons annihilating in

graphitic lattices and mono-vacancies. The XRD results (see figure A3) also showed the existence of highly ordered crystalline phase. The longest lifetime ( $\tau_3$ ) of  $>2$  ns is due to positronium (Ps) annihilation in even bigger voids and internal spaces with a diameter of  $\sim 0.6$  nm. Overall, there is significant crystallinity in the virgin NBG-10, but with many structural voids and positron trapping defects.

From both free and fixed lifetime fittings, the PALS fitting results of L25 showed only one robust positron lifetime ( $\tau_2$ ) of 368 ps with a dominating intensity of 98.3%, which suggests that most of the positrons are trapped and annihilate in one type of vacancies. According to theoretical estimates, this lifetime is most likely due to planar  $V_6$  (i.e., 6 vacancy) clusters, which have also been found in neutron irradiated HOPGs and are quite stable in the annealing experiments. The much narrower pore-size distribution of L25 from the continuum fittings using CONTIN (see Fig. 2) is consistent with the discrete lifetime fitting result and indicates that the concentration of the  $V_6$  clusters is high enough so that the trapping of positrons is ubiquitous (saturated trapping).

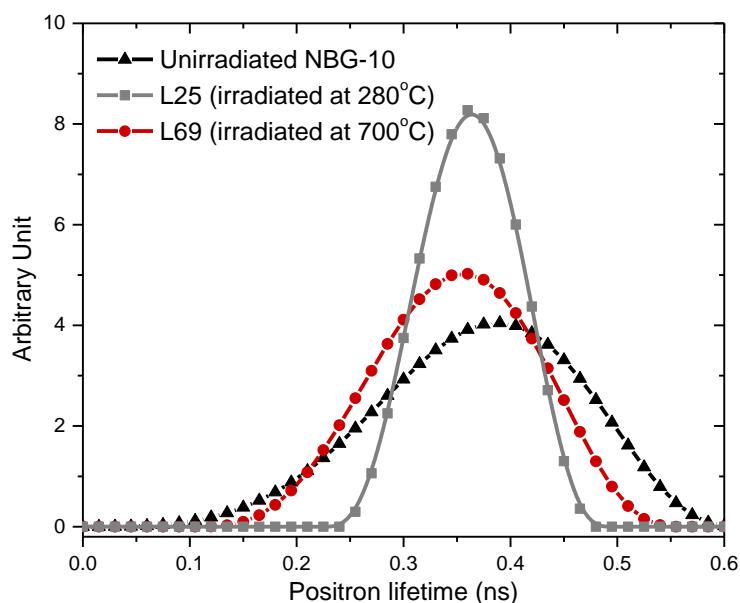


**Fig. 2 - PALS Results for Nuclear Graphite**

With stark contrast to L25, the PALS analysis results of L69 look similar to the virgin NBG-10 with some interesting differences. In the L69 sample, the observed  $\tau_1$  at 235 ps is consistent with positrons annihilating in mono-vacancies. The  $\tau_2$  ( $397 \pm 5$ ps) of L69 is smaller than the positron lifetime in internal surfaces seen in the unirradiated NBG-10, but bigger than the positron lifetime in  $V_6$  vacancy clusters. One interpretation would be that this lifetime is due to the resultant of annihilating in both types of environments. However, we could not rule out the possibility that a variety of voids with different sizes may also play a role. This approach of  $\tau_2$  to

the unirradiated NBG-10 value is consistent with X-ray powder diffraction (XRD) observations indicating that at 700°C the ordered structure was largely preserved (see Fig. 3).

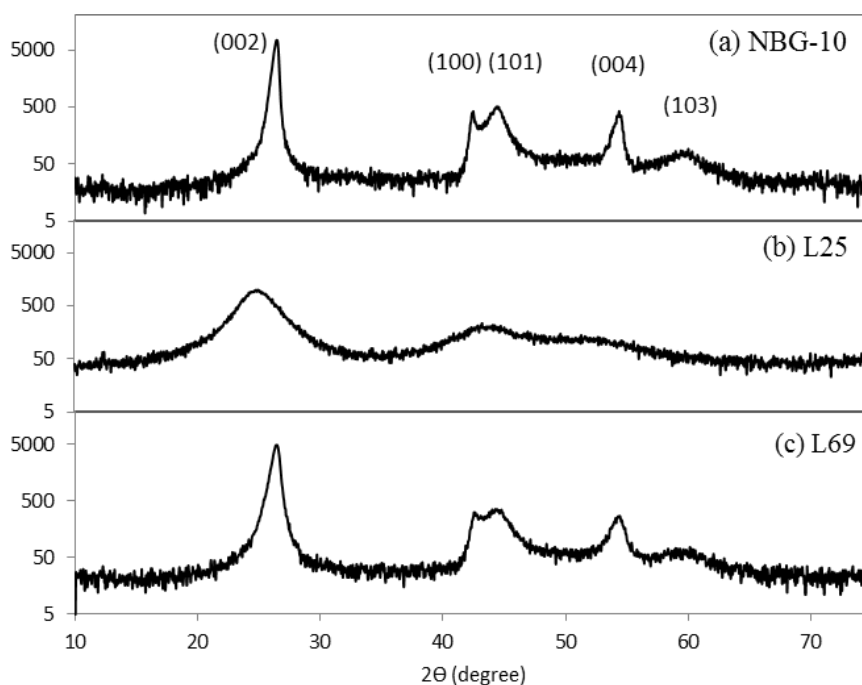


**Fig. 3 - (a) The XRD pattern of unirradiated NBG-10 showing the presence of the crystalline phase. (b) XRD pattern after irradiation at 280°C. (c) The diffraction pattern after irradiation at 700°C.**

The observations at 700°C can be interpreted as a result of the interstitial-vacancy recombination due to the enhanced mobility of the interstitials or interstitial loops. Seemingly, irradiated at 700°C, the vacancies recombine with the interstitials more easily, competing with the process of forming energetically stable  $V_6$  clusters. This interstitial-vacancy recombination has also been observed in other positron and SEM studies. Interestingly, unlike the pristine NBG-10 and L25, L69 has almost no Ps formation ( $\tau_3$ ). This small Ps component change is related to even bigger voids that are probably sensitive to the overall density change. Neutron irradiation at low temperature has a certain swelling effect, which was attributed to the relaxation of internal stresses and has been observed in the macroscopic volume change of nuclear graphite. While annealed at 700°C, these voids are mobile enough so that the structure can shrink to a better packing indicated by the complete loss of all Ps component. Results of continuum lifetime fittings showed that the L25 sample has a narrow distribution centered at  $\sim 370$  ps. It is clear that both NBG-10 and L69 has much broader vacancy size distributions.

In summary, Vacancy-type defects and nanostructural changes in reactor-grade graphite (NGB-10) were examined using PALS after fast neutron irradiation at different temperatures.

## NORTH CAROLINA STATE UNIVERSITY

---

Furthermore, the neutron irradiation at low temperature (280°C) induced significant concentration of  $V_6$  clusters that form in a graphitic plane, concomitantly with the loss of the ordered graphitic structure. Same amount of irradiation at a higher temperature (700°C) caused more noticeable mono-vacancies and the ordered crystalline structure was largely preserved.